


## Review

# Lead-Free Halide Perovskite Nanocrystals for Light-Emitting Diodes

Do-Young Kim <sup>1,2</sup>, Jae-Geun Jung <sup>1,2</sup>, Ye-Ji Lee <sup>1</sup> and Min-Ho Park <sup>1,2,3,\*</sup> 

<sup>1</sup> Department of Materials Science and Engineering, Soongsil University, 369 Sangdo-Ro, Dongjak-Gu, Seoul 06978, Republic of Korea; kdy2269@gmail.com (D.-Y.K.); qwert59211@gmail.com (J.-G.J.); leeyejeje@gmail.com (Y.-J.L.)

<sup>2</sup> Department of Green Chemistry and Materials Engineering, Soongsil University, 369 Sangdo-Ro, Dongjak-Gu, Seoul 06978, Republic of Korea

<sup>3</sup> Integrative Institute of Basic Science, Soongsil University, 369 Sangdo-Ro, Dongjak-Gu, Seoul 06978, Republic of Korea

\* Correspondence: minhopark@ssu.ac.kr

**Abstract:** Lead-based halide perovskite nanocrystals (PeNCs) have demonstrated remarkable potential for use in light-emitting diodes (LEDs). This is because of their high photoluminescence quantum yield, defect tolerance, tunable emission wavelength, color purity, and high device efficiency. However, the environmental toxicity of Pb has impeded their commercial viability owing to the restriction of hazardous substances directive. Therefore, Pb-free PeNCs have emerged as a promising solution for the development of eco-friendly LEDs. This review article presents a detailed analysis of the various compositions of Pb-free PeNCs, including tin-, bismuth-, antimony-, and copper-based perovskites and double perovskites, focusing on their stability, optoelectronic properties, and device performance in LEDs. Furthermore, we address the challenges encountered in using Pb-free PeNC-LEDs and discuss the prospects and potential of these Pb-free PeNCs as sustainable alternatives to lead-based PeLEDs. In this review, we aim to shed light on the current state of Pb-free PeNC LEDs and highlight their significance in driving the development of eco-friendly LED technologies.

**Keywords:** halide perovskite light-emitting diodes; lead-free halide perovskite nanocrystals; perovskite nanocrystal emitters; eco-friendly perovskite nanocrystals



**Citation:** Kim, D.-Y.; Jung, J.-G.; Lee, Y.-J.; Park, M.-H. Lead-Free Halide Perovskite Nanocrystals for Light-Emitting Diodes. *Materials* **2023**, *16*, 6317. <https://doi.org/10.3390/ma16186317>

Academic Editor: Zhonglin Du

Received: 13 August 2023

Revised: 11 September 2023

Accepted: 18 September 2023

Published: 20 September 2023



**Copyright:** © 2023 by the authors. Licensee MDPI, Basel, Switzerland. This article is an open access article distributed under the terms and conditions of the Creative Commons Attribution (CC BY) license (<https://creativecommons.org/licenses/by/4.0/>).

## 1. Introduction

In recent years, metal halide perovskites (MHPs) have received considerable attention as highly promising materials for a range of optoelectronic applications, including solar cells, light-emitting diodes (LEDs), photodetectors, lasers, and photocatalysts [1–12]. Notably, lead (Pb)-based halide perovskites (LHPs) have emerged as particularly appealing. This is due to their exceptional optoelectronic properties, which are characterized by high photoluminescence quantum yield (PLQY), long carrier diffusion length, high charge carrier mobility, high defect tolerance, and narrow emission spectra [13–20]. These properties make these materials highly promising candidates for next-generation LEDs. Moreover, a reduction in the crystal size toward the nanometer scale has a substantial impact on the material properties, thereby enabling deliberate adjustment of the optoelectronic characteristics [21–25]. Applications of MHP nanocrystals (PeNCs) have already been established in various fields [26–32], and their device applications are expected to be commercialized.

However, the presence of Pb<sup>2+</sup> in LHPs poses significant challenges to their widespread commercialization. Pb<sup>2+</sup> is highly soluble in water, which introduces potential risks to the environment and human health throughout the product life cycle, including disposal. Exposure to Pb can result in various adverse health effects, including neurological disorders, gastrointestinal issues, insomnia, coma, and convulsions. The inherent toxicity of Pb raises concerns regarding its environmental impact and human safety, making LHPs incompatible

with the restriction of hazardous substances (RoHS) directive and industrial reliability standards [33–35]. Therefore, there has been growing interest, and various research efforts have focused on exploring and developing Pb-free PeNCs as promising alternatives to address these intrinsic challenges.

The development of Pb-free perovskites is a crucial alternative strategy for the commercialization of MHP-based devices by substituting Pb cations with nontoxic metal cations, such as tin (Sn), bismuth (Bi), antimony (Sb), or transition metals such as copper (Cu). To achieve this goal, researchers have aimed to eliminate toxicity concerns associated with Pb while achieving comparable or enhanced optoelectronic performance [36–40].

In this review, we provide a comprehensive overview of recent advances in Pb-free PeNCs for LED (PeNC-LED) applications. We discuss the synthetic strategies employed for the development of Pb-free PeNCs, including the selection of nontoxic metal cations and the optimization of crystal structures. Additionally, we examine the optoelectronic properties of Pb-free PeNCs, such as their photoluminescence (PL) characteristics, band structure, and emission mechanism. Moreover, we explore the strategies employed to enhance the stability and operational lifetime of Pb-free PeNC-LEDs and discuss the challenges by addressing key research directions and prospects for the development of Pb-free PeNC-LEDs.

## 2. B-Site Metal Candidates for Pb-Free Perovskite Nanocrystals

In the context of traditional LHPs, the general chemical formula can be expressed as  $ABX_3$ , wherein A represents an inorganic monocation such as  $Cs^+$ ,  $Rb^+$ , or  $K^+$  and an organic monocation such as the methylammonium cation ( $MA^+$ ) and the formamidinium cation; B denotes a bivalent  $Pb^{2+}$  ion; and X represents halide ions such as  $Cl^-$ ,  $Br^-$ , or  $I^-$  [41,42]. The stability of three-dimensional (3D)  $ABX_3$  perovskite structures can be evaluated using Goldschmidt's tolerance factor  $t$  (1) and the octahedral factor  $\mu$  (2):

$$t = \frac{r_A + r_X}{\sqrt{2}(r_B + r_X)} \quad (1)$$

$$\mu = \frac{r_B}{r_X} \quad (2)$$

where  $r_A$ ,  $r_B$ , and  $r_X$  correspond to the ionic radii A, B, and X, respectively. Stable perovskite crystal structures are formed when these two factors are in the ranges of  $0.8 \leq t \leq 1.0$  and  $0.44 \leq \mu \leq 0.90$  [41,43–45]. However, as the ionic radius of the A-site cation increases, which leads to a larger tolerance factor, lower-dimensional perovskite structures are formed [46–48]. Such dimensions and crystal structure variations result in MHPs having diverse band structures and photophysical and optoelectronic properties, making them promising candidates for various applications. Figure 1 shows the elements in the periodic table denoted by distinct colors (A-site: green, B-site: sky-blue, and X-site: orange), considered potentially viable or having been employed at the A, B, and X positions of the MHPs [49–54]. Extensive research is being conducted on MHPs with various compositions to progressively enhance their performance across diverse fields.

Furthermore, MHPs based on toxic metals, such as Pb and Cd, encounter challenges for commercialization owing to the RoHS directive. Thus, research on Pb-free MHPs is essential for their industrial applications. To substitute non-toxic metals for toxic Pb in LHPs, attention should be paid to the ionic radius and charge neutrality of the substituting metal elements. The selection of elements must satisfy the requirements of an appropriate ionic radius to maintain the structural integrity of the perovskite lattice. Moreover, substitutions should ensure charge neutrality within the crystal structure to maintain overall electrostatic balance [55]. By carefully considering these factors, it is possible to identify suitable elements for effective Pb substitution in LHPs. This leads to the development of Pb-free MHPs with the desired properties for optoelectronic device applications, including LEDs. Among the promising elemental candidates, we focus on Sn-, Bi-, Sb-, Cu-based, and double PeNCs and provide an overview of their applications in PeNC-LEDs.



1	2	3	4	5	6	7	8	9	10	11	12	13	14	15	16	17	18
1 H																	2 He
3 Li	4 Be											5 B	6 C	7 N	8 O	9 F	10 Ne
11 Na	12 Mg											13 Al	14 Si	15 P	16 S	17 Cl	18 Ar
19 K	20 Ca	21 Sc	22 Ti	23 V	24 Cr	25 Mn	26 Fe	27 Co	28 Ni	29 Cu	30 Zn	31 Ga	32 Ge	33 As	34 Se	35 Br	36 Kr
37 Rb	38 Sr	39 Y	40 Zr	41 Nb	42 Mo	43 Tc	44 Ru	45 Rh	46 Pd	47 Ag	48 Cd	49 In	50 Sn	51 Sb	52 Te	53 I	54 Xe
55 Cs	56 Ba		72 Hf	73 Ta	74 W	75 Re	76 Os	77 Ir	78 Pt	79 Au	80 Hg	81 Tl	82 Pb	83 Bi	84 Po	85 At	86 Rn
87 Fr	88 Ra		104 Rf	105 Db	106 Sg	107 Bh	108 Hs	109 Mt	110 Ds	111 Rg	112 Cn	113 Nh	114 Fl	115 Mc	116 Lv	117 Ts	118 Og

57 La	58 Ce	59 Pr	60 Nd	61 Pm	62 Sm	63 Eu	64 Gd	65 Tb	66 Dy	67 Ho	68 Er	69 Tm	70 Yb	71 Lu
89 Ac	90 Th	91 Pa	92 U	93 Np	94 Pu	95 Am	96 Cm	97 Bk	98 Cf	99 Es	100 Fm	101 Md	102 No	103 Lr

**Figure 1.** Periodic table of the elements that have the potential to constitute perovskite compositions (A-site: green; B-site: sky-blue; and X-site: orange).

### 2.1. Sn-Based Perovskite Nanocrystals

Sn belongs to group 14 of the periodic table, which is the same group as Pb, and possesses an equivalent valence configuration, resulting in the ability to retain electrical neutrality within the  $ABX_3$  crystal structure (Figure 2a). Moreover, Sn cations have an ideal cubic structure surrounded by an octahedron of anions. These characteristics have led to extensive investigations into Sn as a promising B-site metal replacement for Pb. However,  $ABX_3$ -structured Sn-based perovskites have been observed to spontaneously undergo rapid decolorization and conversion to the  $A_2BX_6$  formula after exposure to atmospheric conditions, implying a rapid degradation phenomenon [56]. Such structural changes adversely affect the chemical and luminescence properties of Sn-based PeNCs (Sn-PeNCs) [57]. Therefore, significant efforts have been made in recent years to investigate the structural and luminescent properties of Sn-PeNCs.

Precise control of the precursor ratios over various ranges is crucial for achieving a low density of structural defects within the lattice of the  $CsSnX_3$  NCs [58]. This is because the defect formation energy is intricately linked to the chemical potential of each constituent involved in the reaction. Figure 2b shows bright-field transmission electron microscopy (TEM) images of  $CsSnI_3$  NCs with different Cs:Sn ratios. As the Sn content increases, the average size of the cubic  $CsSnI_3$  NCs also increases. For instance, an average size of 26 nm was obtained at a Cs:Sn ratio of 0.25:3 and 37 nm at a ratio of 0.25:4.8. Additionally, byproducts, which are presumed to be unreacted species or reaction intermediates, were observed in  $CsSnX_3$  NCs with a ratio of 0.25:4.8. Furthermore, at the higher Sn ratio of 4.8, large crystals exceeding 200 nm were formed, larger than those at ratios of 3, 3.6, and 4.2. These results indicate that the precursor ratio plays a crucial role in determining the size distribution and purity of  $CsSnI_3$  NCs during synthesis.

By consistently addressing the challenge of preventing the oxidation of Sn(II) to Sn(IV), the performance of Sn-based MHPs has demonstrated consistent improvement. The low stability of CsSnBr<sub>3</sub> NCs can be enhanced by the precise synthesis of CsSnBr<sub>3</sub> cubic nanocages, which uses a simple hot-injection colloidal approach [59]. The fabrication of the nanocages can be carefully regulated by selecting suitable precursors, such as MgBr, and adjusting the reaction temperature, resulting in their formation through a self-assembly-driven process. MgBr was used as the bromide source because Mg<sup>2+</sup> has a smaller ionic radius, which, according to tolerance factor theory, prevents its penetration into the perovskite structure. Uncoordinated 1-octadecene (ODE) was chosen as the solvent, and oleic acid (OA) and oleylamine (OAm) were selected as ligands. During this process, injection of the Cs-oleate precursor into the Sn-Br precursor solution resulted in a rapid color change, turning the solution dark red within a few seconds. This color transformation indicates the successful formation of CsSnBr<sub>3</sub> nanocages.

A surface treatment with perfluorooctanoic acid (PFOA) also substantially enhanced the stability of CsSnBr<sub>3</sub> cubic nanocages [59]. PFOA exhibits a stronger electron-withdrawing capability than Br<sup>−</sup>, which passivates the surface of the CsSnBr<sub>3</sub> nanocages. It forms a stronger interaction with Sn<sup>2+</sup>, effectively hindering oxidation. Additionally, PFOA induces steric hindrance, further enhancing the stability of the CsSnBr<sub>3</sub> nanocages. As shown in Figure 2c, the pristine CsSnBr<sub>3</sub> nanocage films show gradual disintegration, with approximately 30% decomposition after 48 h under various desiccation conditions, whereas the PFOA-functionalized CsSnBr<sub>3</sub> nanocage film exhibits a relatively slow decomposition rate of 25% in a moisture-free environment. When the films were exposed to illumination, the pristine CsSnBr<sub>3</sub> films degraded rapidly, with over 95% decomposition within 24 h. Conversely, the PFOA-functionalized CsSnBr<sub>3</sub> film exhibited a slight degradation of approximately 10% under the same conditions. Therefore, water is a critical factor that directly influences the stability of CsSnBr<sub>3</sub> nanocages, and exposure to light accelerates degradation by the decomposition process.

Surface passivation using polymers is another effective strategy for enhancing the stability of Sn-PeNCs [60–62]. The incorporation of gelatin, an amphoteric polymer obtained as a partial product of collagen hydrolysis, is crucial for providing resistance against water degradation [61]. The hygroscopic nature of the gelatin network effectively stabilizes and protects CsSnCl<sub>3</sub> NCs from water-induced damage. Moreover, the high molecular weight of gelatin allows tight coating and isolation of the PeNCs, effectively suppressing self-aggregation and oxidation.

Accordingly, gelatin-coated CsSnI<sub>3</sub> nanocrystals (gel-CsSnI<sub>3</sub> NCs) have been shown to exhibit notably enhanced stability under harsh environmental conditions when compared to pristine OA/OAm-based CsSnI<sub>3</sub> NCs (Figure 2d). The PL intensity of the gel-CsSnI<sub>3</sub> NCs was maintained above 93.28% and 85% for 72 h under dark conditions and UV irradiation, respectively (pink and green lines). By contrast, the water resistance test revealed that the PL stability of pristine CsSnI<sub>3</sub> NCs degraded by over 95% within 5 min. The low stability of pristine CsSnI<sub>3</sub> NCs could originate from the addition of water to the PeNC solution in cyclohexane, resulting in delamination, ligand loss, self-aggregation, PL quenching, and even decomposition. On the contrary, the PL intensity of gel-CsSnI<sub>3</sub> NCs exhibited minimal change after 5 min (Figure 2d, inset) and remained above 75% after 72 h (blue line).

Based on these results, Figure 2e presents a schematic of the proposed interaction mechanism between the gelatin and CsSnCl<sub>3</sub> NCs. The interaction between gelatin and the CsSnCl<sub>3</sub> NCs involves the coordination of the carboxylate and amino groups of gelatin with the Sn atoms in the NCs. Additionally, the protonated amino groups form hydrogen bonds with the Cl atoms. The numerous functional groups in gelatin lead to the occupation of active sites on the NC surface, creating a “rich ligand” state. As a result, comprehensive passivation of the NC surface by gelatin effectively inhibits the formation of surface defects. Therefore, the surface passivation strategy enhances the stability of Sn-PeNCs under atmospheric conditions, highlighting their potential for various applications.

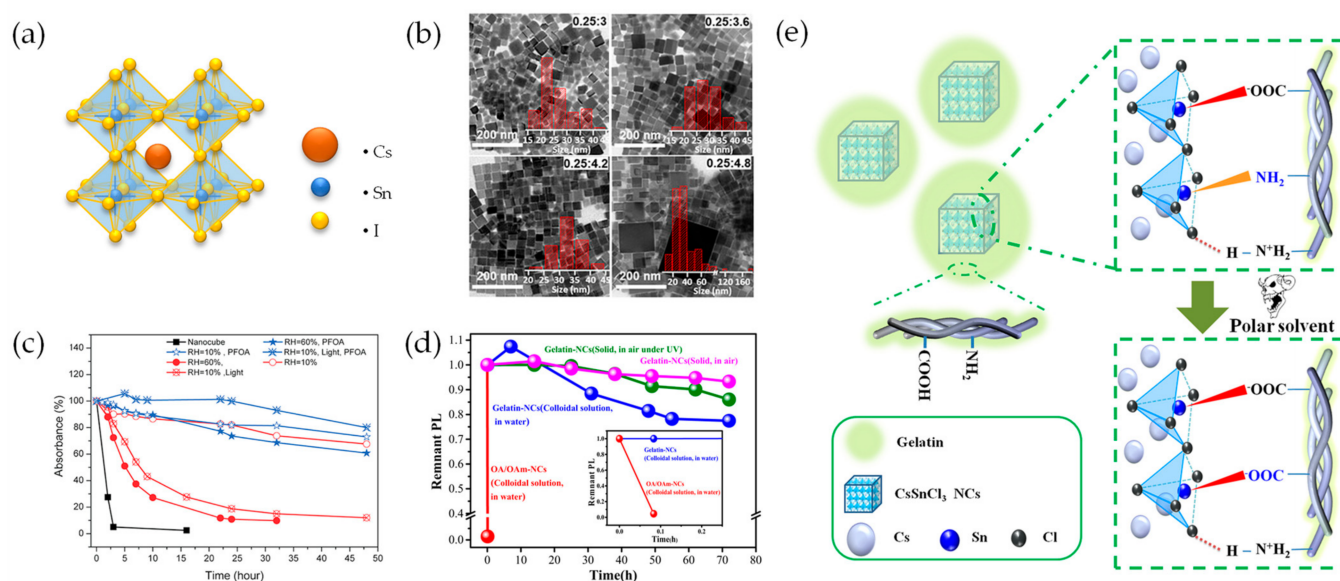


**Figure 2.** (a) Crystal structure of CsSnI<sub>3</sub>; (b) TEM images of CsSnI<sub>3</sub> PeNCs with different ratios of Cs:Sn. Insets indicate histograms of the average particle size of each CsSnI<sub>3</sub> NC; (b) Reprinted with permission from Ref. [58]. Copyright, 2021 American Chemical Society. (c) The variation of absorbance over time intensity at 620 nm under various conditions. The temperature and light intensity were 25 °C and 1200 mW/cm<sup>2</sup> for all measurements; (e) Reprinted with permission from Ref. [59]. Copyright, 2017 American Chemical Society. (d) Remnant PL values of gelatin-NCs and oleic acid (OA)/oleylamine (OAm)-NCs over time under exposure to air, UV irradiation, and water. (Inset: remnant PL of gelatin-NCs and OA/OAm-NCs in 0.1 h). (e) Schematic image of gelatin coordinate with Sn in CsSnI<sub>3</sub> NCs; (d,e) Reprinted with permission from Ref. [61]. Copyright 2020, Elsevier.

Sn-PeNCs have been extensively studied as environmentally friendly Pb-free PeNCs due to their promising characteristics, including the same ns<sup>2</sup> valence electron configuration and similar ion radii (Sn:1.35 Å, Pb:1.49 Å). They enable the substitution of Pb cations within the ABX<sub>3</sub> structure while maintaining charge neutrality [63]. To enhance their structural stability, numerous studies have been conducted on controlling precursor ratios and surface engineering through the introduction of additives such as perfluoroalkyl acids and polymers. However, their practical applications have been limited owing to a lack of research on suitable additives for preventing Sn oxidation. Consequently, current research efforts have focused on enhancing the stability of Sn-PeNCs by exploring additives that can effectively inhibit Sn oxidation.

## 2.2. Bi-Based Perovskite Nanocrystals

The electronic properties of the LHPs can be attributed to the electronic configuration of Pb<sup>2+</sup>, which is characterized as 6s<sup>2</sup>6p<sup>0</sup>. This configuration enables the hybridization of the Pb 6s orbital with the halogen *p* orbital for valence band formation and of the Pb 6p orbitals with halogen *p* orbitals for conduction bands. This leads to the observed electronic properties. The presence of shallow defect states in LHPs is closely linked to the strong antibonding interactions that occur between the Pb 6s and halide 5p orbitals within the valence band [64,65].

Bi, which belongs to the same period as Pb, possesses a cationic electron configuration similar to that of Pb<sup>2+</sup>, featuring a [Xe] 4f<sup>14</sup>5d<sup>10</sup>6s<sup>2</sup> electron arrangement. The presence of a 6s<sup>2</sup> lone pair is a distinctive characteristic of Bi that enables it to displace Pb by a heterogeneous substitution mechanism, resulting in the replacement of Pb<sup>2+</sup> with Bi<sup>3+</sup> [66]. Moreover, Bi is an eco-friendly alternative to Pb, offering low toxicity and high stability [67–70].

When Bi replaces Pb in LHPs, maintaining electrical neutrality requires the substitution of three  $\text{Pb}^{2+}$  ions with two  $\text{Bi}^{3+}$  ions, leading to the formation of  $\text{A}_3\text{B}_2\text{X}_9$  structures within the  $\text{ABX}_3$  framework. Leng et al. first reported the synthesis of  $\text{MA}_3\text{Bi}_2\text{Br}_9$  NCs that exhibited an emission wavelength of 430 nm and a maximum PLQY of 12% [71]. Subsequently, numerous studies have been conducted on the synthesis of Bi-PeNCs [69–74]. However, the inconsistent optical properties observed for various colloidal Bi-PeNC synthesis methods indicate the presence of various crystal structures. The combination of  $\text{Cs}^+$  and  $\text{Bi}^{3+}$  cations with halide anions can generate  $\text{Cs}_3\text{BiX}_6$  and  $\text{Cs}_3\text{Bi}_2\text{X}_9$  (Figure 3a) [75].  $\text{Cs}_3\text{Bi}_2\text{Br}_9$  possesses a two-dimensional (2D) layered structure in the  $\text{P}\bar{3}\text{m}1$  space group, and one-third of its B-site cation positions are replaced by vacancies. By contrast, dimer structures such as  $\text{Cs}_3\text{Bi}_2\text{I}_9$  are formed by  $\text{Cs}^+$  or  $\text{MA}^+$  cations in the face-sharing octahedra and belong to the  $\text{P}6_3/\text{mmc}$  space group. The bandgap calculated by density functional theory (DFT) using the Vienna ab initio simulation package indicates that the layered structure has a smaller bandgap than the dimer structure, which can be attributed to its smaller lattice constant and volume [76,77]. By changing the A-site in  $\text{Cs}_3\text{Bi}_2\text{I}_9$  from  $\text{Cs}^+$  to  $\text{Rb}^+$  or  $\text{K}^+$ , the transformation from a dimer to a layered structure can be observed, leading to a transition from an indirect bandgap to a direct bandgap. However, when  $\text{Rb}^+$  or  $\text{K}^+$  cations are used at the A-site of the  $\text{A}_3\text{Bi}_2\text{I}_9$  structure, the smaller size of these ions results in a lower-symmetry distorted lattice with the  $\text{P}2_1/\text{n}$  space group [78].

To investigate the bandgap characteristics associated with the  $\text{Cs}_3\text{Bi}_2\text{I}_9$  crystal structure, colloidal  $\text{Cs}_3\text{BiX}_6$  and  $\text{Cs}_3\text{Bi}_2\text{X}_9$  NCs were synthesized using the hot-injection method and anion exchange with trimethylsilyl halides ( $\text{TMS-X}$ ) [75]. The direct synthesis of  $\text{Cs}_3\text{Bi}_2\text{I}_9$  leads to the formation of a dimer rather than a layered structure [79–81]. Because the direct synthesis of layered  $\text{Cs}_3\text{Bi}_2\text{I}_9$  is challenging, layered  $\text{Cs}_3\text{Bi}_2\text{I}_9$  can be achieved through anion exchange with  $\text{TMS-I}$ . When comparing the optical properties of dimeric  $\text{Cs}_3\text{Bi}_2\text{I}_9$  with those of layered  $\text{Cs}_3\text{Bi}_2\text{I}_9$ , it was observed that the first absorption peak in dimeric  $\text{Cs}_3\text{Bi}_2\text{I}_9$  appeared at 492 nm, while a similar transition in layered  $\text{Cs}_3\text{Bi}_2\text{I}_9$  appeared to be red-shifted to 550 nm (Figure 3b). Layered  $\text{Cs}_3\text{Bi}_2\text{I}_9$  exhibits distinctive peaks that differ from dimeric  $\text{Cs}_3\text{Bi}_2\text{I}_9$ , although the powder X-ray diffraction (XRD) patterns do not entirely exclude the presence of dimeric structures in the layered phase (Figure 3c). Additionally, band structure calculations using plane-wave DFT revealed that the band gap of the layered structure is lower than that of the dimeric structure. This observation is attributed to the lower conduction band minimum (CBM) in the layered structure compared to that in the dimer structure, resulting in a reduction in the bandgap. The crystal structure of Bi-PeNCs can be influenced by the heating-up process, which is commonly employed for the synthesis of colloidal inorganic quantum dots (QDs). This is because it induces the nucleation, growth, and crystallization of inorganic QDs at high temperatures. The heating-up synthesis method provides relative safety owing to the absence of injection at high temperatures and the controllability of the crystal size by varying the reaction temperature and time, making it potentially advantageous for large-scale production [82–86]. Building on this approach, heating-up synthesis without injection can be used to synthesize cesium bismuth bromide NCs [87]. A mixture of  $\text{CsBr}$ ,  $\text{BiBr}_3$ , OA, and OAm was stirred in ODE under vacuum, followed by heat treatment, resulting in the synthesis of  $\text{Cs}_3\text{BiBr}_6$  or  $\text{Cs}_3\text{Bi}_2\text{Br}_9$  NCs. The structure of cesium bismuth bromide NCs can transform from  $\text{Cs}_3\text{BiBr}_6$  to  $\text{Cs}_3\text{Bi}_2\text{Br}_9$ , depending on the temperature and amount of OA. The PL and PL excitation (PLE) spectra of  $\text{Cs}_3\text{BiBr}_6$  and  $\text{Cs}_3\text{Bi}_2\text{Br}_9$  are shown in Figure 3d and 3e, respectively. The emission peak of  $\text{Cs}_3\text{BiBr}_6$  is observed at 435 nm, whereas that of  $\text{Cs}_3\text{Bi}_2\text{Br}_9$  is red-shifted to 461 nm. The absorption spectra corresponded to a bandgap of 3.05 and 2.67 eV, respectively.

Metal-cation doping is an efficient approach for enhancing the optoelectronic properties of PeNCs. Liu et al. synthesized  $\text{Mn}^{2+}$ -doped  $\text{Cs}_3\text{Bi}_2\text{I}_9$  NCs to improve these properties [88]. In this method,  $\text{MnI}_2$  was added to the Bi-oleate solution, and the addition of  $\text{Mn}^{2+}$  ions suppressed and eliminated the formation of  $\text{CsI}$  impurities arising from the decomposition of the intermediate  $\text{Cs}_3\text{BiI}_6$  species during synthesis. Figure 3f shows the absorption and PL spectra as a function of the  $\text{Mn}^{2+}$  doping concentration. Compared with the absorption spectrum



of the undoped  $\text{Cs}_3\text{Bi}_2\text{I}_9$  NCs, that of  $\text{Mn}^{2+}$ -doped  $\text{Cs}_3\text{Bi}_2\text{I}_9$  was red-shifted, accompanied by double peaks at 530–540 and 610–620 nm. This can be attributed to emission from a spin-forbidden  ${}^4\text{T}_1\text{-}{}^6\text{A}_1$  Mn d-d transition resulting from the transfer of exciton energy from the host  $\text{Cs}_3\text{Bi}_2\text{I}_9$  to the  $\text{Mn}^{2+}$  dopants, as commonly observed in  $\text{Mn}^{2+}$ -doped LHP NCs [89–91]. Additionally, with increasing  $\text{Mn}^{2+}$  concentration from 1 to 5%, the intensity of the PL spectrum increased with a small spectral blue shift from 620 to 610 nm and an improved PLQY from 0.54% (undoped) to 1.57% (5% doped). Figure 3g illustrates the emission mechanism of the  $\text{Mn}^{2+}$ -doped  $\text{Cs}_3\text{Bi}_2\text{I}_9$  NCs. When the  $\text{Mn}^{2+}$ -doped  $\text{Cs}_3\text{Bi}_2\text{I}_9$  NCs were excited at  $\sim 510$  nm, energy was transferred from the  $\text{Cs}_3\text{Bi}_2\text{I}_9$  host to the  $\text{Mn}^{2+}$  dopants, resulting in emission from the  $\text{Mn}^{2+}$ . Exciton relaxation occurs through three pathways: (i) recombination within the host material assisted by phonons; (ii) non-radiative recombination involving trap sites; and (iii) radiative emission through the Mn d-d transition ( ${}^4\text{T}_1\text{-}{}^6\text{A}_1$ ), facilitated by energy transfer to  $\text{Mn}^{2+}$ . Through these exciton relaxation pathways, the  $\text{Mn}^{2+}$ -doped  $\text{Cs}_3\text{Bi}_2\text{I}_9$  NCs exhibited two emission peaks attributed to radiative recombination within the  $\text{Cs}_3\text{Bi}_2\text{I}_9$  host and  $\text{Mn}^{2+}$  dopants, and an increase in radiative recombination leads to an enhanced PLQY.

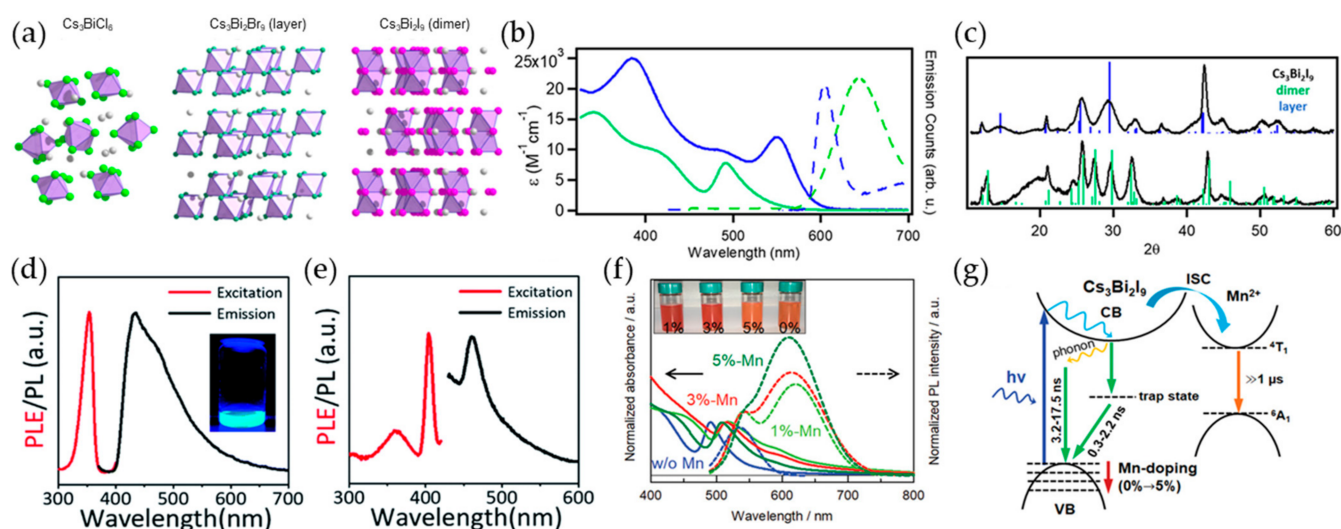


**Figure 3.** (a) Crystal structures of  $\text{Cs}_3\text{BiCl}_6$ ,  $\text{Cs}_3\text{Bi}_2\text{Br}_9$ , and  $\text{Cs}_3\text{Bi}_2\text{I}_9$  in bulk; (b) extinction coefficient (solid lines) and PL (dashed lines) spectra for  $\text{Cs}_3\text{Bi}_2\text{I}_9$  polymorphs (blue: layered, green: dimer); (c) Powder X-ray diffraction (XRD) patterns for  $\text{Cs}_3\text{Bi}_2\text{I}_9$  polymorphs; (a–c) reprinted with permission from Ref. [75]. Copyright 2019, American Chemical Society. (d) PL excitation (PLE) and PL spectrum of  $\text{Cs}_3\text{BiBr}_6$  NCs. PL at an excitation wavelength of 360 nm and PLE at an emission wavelength of 440 nm; (e) PL and PLE spectra of  $\text{Cs}_3\text{Bi}_2\text{Br}_9$  NCs. PL under an excitation wavelength of 358 nm and PLE at an emission wavelength of 461 nm; (d,e) reprinted with permission from Ref. [87]. Copyright 2020, Royal Society of Chemistry. (f) Absorption (solid lines) and PL (dashed lines) spectra of different levels of Mn-doped  $\text{Cs}_3\text{Bi}_2\text{I}_9$  NCs, respectively. Inset: the appearance of different Mn-doped  $\text{Cs}_3\text{Bi}_2\text{I}_9$  NCs; (g) emission mechanisms of  $\text{Cs}_3\text{Bi}_2\text{I}_9$  with  $\text{Mn}^{2+}$  doping; (f,g) reprinted with permission from Ref. [88]. Copyright 2021, Wiley-VCH.

Despite significant progress in the field of Bi-PeNCs, their PLQY remains generally low [69–72,75,87,92]. This is primarily attributed to residual surface states, strong photon-phonon coupling, and dangling bonds present on the PeNC surfaces [93,94]. To address this issue, the synthesis of  $\text{MA}_3\text{Bi}_2(\text{Cl}, \text{Br})_9$  NCs was proposed through a collaborative ligand-assisted reprecipitation (Co-LARP) method, which leads to an improvement in the PLQY through surface passivation [95]. The added Cl anions serve as ligands on the surface of the PeNCs, reducing surface defects and inducing a blue-shifted emission spectrum. Notably, when the  $\text{Cl}/(\text{Cl} + \text{Br})$  ratio reached 33%, the  $\text{MA}_3\text{Bi}_2(\text{Cl}, \text{Br})_9$  NCs exhibited a



maximum PLQY of 54.1%, and the PL intensity remained at 88% after 12 h under 365 nm UV irradiation.

Bi-PeNCs exhibit various crystal structures depending on their constituent elements. Their optical, photophysical, and electronic properties can be altered using different synthesis methods and doping strategies. Various approaches offer the potential for advancement by tuning and enhancing their optoelectronic characteristics. Although there are no reported cases of Bi-PeNC-based LEDs and their optical properties are inferior to those of LHP NCs, the low cost, non-toxicity, and high stability of Bi suggest that Bi-PeNCs are promising candidates for Pb replacement.

### 2.3. Sb-Based Perovskite Nanocrystals

$\text{Cs}_3\text{Sb}_2\text{X}_9$  ( $\text{X} = \text{Cl}, \text{Br}, \text{and I}$ ), which has a trigonal crystal structure with space group  $\text{P}\bar{3}\text{m1}$  (no. 164), consists of two  $[\text{Sb}_2\text{X}_9]^{3-}$  polyhedra within a single unit [96]. In the crystal structure of  $\text{Cs}_3\text{Sb}_2\text{X}_9$  shown in Figure 4a, two  $\text{Sb}^{3+}$  ions are located on the body diagonal of the unit cell, whereas the eight top corners are occupied by  $\text{Cs}^+$  ions. The connected  $[\text{Sb}_2\text{X}_9]^{3-}$  polyhedra form a bilayer structure that is stacked together.  $\text{Cs}_3\text{Sb}_2\text{X}_9$  has a layered structure and exhibits triangular symmetry.

A simple reprecipitation method did not yield Sb-PeNCs without the assistance of long-chain ligands or excessive ligand usage.  $\text{Cs}_3\text{Sb}_2\text{Br}_9$  NCs can be synthesized using the ligand-assisted reprecipitation (LARP) method. This enables room-temperature PeNC synthesis without traditional heating, an inert gas atmosphere, or injection conditions [97]. LARP involves the direct addition of a reaction precursor solution to a vigorously stirred, poor solvent to rapidly achieve a supersaturated state (Figure 4b). To initiate the LARP synthesis process, a clear precursor solution was prepared by dissolving a mixture of  $\text{SbBr}_3$ ,  $\text{CsBr}$ , and OAm in a good solvent such as *N,N*-dimethylformamide (DMF) or dimethylsulfoxide (DMSO). Subsequently, a fixed quantity of the prepared precursor solution was carefully dropped into a vigorously stirred solution of octane and OA, which serves as a poor solvent for the precursors. Supersaturation induces the immediate and efficient recrystallization of  $\text{Cs}_3\text{Sb}_2\text{Br}_9$  NCs, leading to their successful synthesis. By utilizing a mixture of octane and OA as ligands,  $\text{Cs}_3\text{Sb}_2\text{Br}_9$  NCs with PLQYs of ~20% were synthesized. Moreover, by further optimizing the synthesis conditions of a precursor concentration of 0.033 mM, an octane/OA ratio of 10:1, and a room-temperature reaction, monodispersed  $\text{Cs}_3\text{Sb}_2\text{Br}_9$  NCs were obtained with a high PLQY of 46% and a uniform size of 3.07 nm [98].

This doping strategy was proven to be highly effective in enhancing the optical properties of Sb-PeNCs synthesized by the hot injection method. Pristine  $\text{K}_3\text{SbCl}_6$  NCs displayed a broad PL spectrum associated with self-trapped excitons (STE) and achieved a moderate PLQY of 22.3% [99]. However, through the incorporation of  $\text{Mn}^{2+}$  ions as dopants, the  $\text{Mn}^{2+}$ -doped  $\text{K}_3\text{SbCl}_6$  NCs exhibited a remarkable PLQY improvement to 37.2%, attaining white light emission. Furthermore,  $\text{Mn}^{2+}$ -doped  $\text{K}_3\text{SbCl}_6$  NCs introduce additional red emission associated with the intrinsic transition ( ${}^4\text{T}_1 - {}^6\text{A}_1$ ) of  $\text{Mn}^{2+}$  ions [100,101]. A primary dynamic process for the  $\text{Mn}^{2+}$ -doped  $\text{K}_3\text{SbCl}_6$  NCs was proposed (Figure 4c). Initially, upon excitation, the excited charge carriers cause rapid elastic distortions, leading to the formation of STE states owing to strong electron-phonon interactions within the  $\text{K}_3\text{SbCl}_6$  host. Simultaneously, an energy transfer process occurs between the  $\text{Mn}^{2+}$  dopant ions and the surrounding STE states, resulting in the excitation of the  $\text{Mn}^{2+}$  dopants.

This excitation leads to an efficient red emission spectrum through the intrinsic transitions ( ${}^4\text{T}_1 - {}^6\text{A}_1$ ) of the  $\text{Mn}^{2+}$  ions, contributing to an observed additional red emission in the  $\text{Mn}^{2+}$ -doped  $\text{K}_3\text{SbCl}_6$  NCs. The interplay of these dynamic processes not only enhances the overall PLQY but also induces the versatile luminescent properties of  $\text{Mn}^{2+}$ -doped  $\text{K}_3\text{SbCl}_6$  NCs, offering possibilities for optoelectronic applications. The energy transfer process was further validated using excitation spectra obtained by selectively monitoring the energy transfer from the STE at 440 nm and the intrinsic transition of  $\text{Mn}^{2+}$  ions at 600 nm. Both emission spectra exhibited similar broad excitation bands, confirming the occurrence of energy transfer between these two entities. The emission decay was signif-

icantly faster when the STE was monitored at 440 nm with increasing concentrations of  $\text{Mn}^{2+}$ . This indicates that the excited energy level ( ${}^4\text{T}_1 - {}^6\text{A}_1$ ) of the  $\text{Mn}^{2+}$  ions primarily originates from the energy transferred from the STE of the  $\text{K}_3\text{SbCl}_6$  NCs host. The faster emission decay suggests an efficient energy transfer from the perovskite host to the  $\text{Mn}^{2+}$  ions, confirming the occurrence of energy transfer between them. By controlling the doping concentration of  $\text{Mn}^{2+}$  ions, it was possible to achieve white-light emission with a PLQY of 37.2%. XRD analysis of the 4.2%  $\text{Mn}^{2+}$ -doped  $\text{K}_3\text{SbCl}_6$  NCs revealed that the diffraction peaks at approximately  $15.1^\circ$ ,  $24.4^\circ$ ,  $29.3^\circ$ ,  $34.0^\circ$ , and  $46.0^\circ$  remained similar to those of the undoped  $\text{K}_3\text{SbCl}_6$  NCs (Figure 4d). These diffraction peaks are associated with the zero-dimensional (0D) monoclinic  $\text{K}_3\text{Sb}_2\text{Cl}_6$  perovskite structure (PDF#24-0833). Interestingly, the diffraction peaks of the  $\text{Mn}^{2+}$ -doped  $\text{K}_3\text{SbCl}_6$  NCs showed minimal changes at  $\text{Mn}^{2+}$  ion doping concentrations of 0.12%, 1.5%, and 3.7%, and a clear red shift in the diffraction peaks was observed when the  $\text{Mn}^{2+}$  ion doping concentration exceeded 4.2%. This observation provides further evidence that  $\text{Mn}^{2+}$  ions were successfully incorporated into the lattice of the 0D  $\text{K}_3\text{SbCl}_6$  host. Furthermore, the relative intensity of the STE emission, compared to the intrinsic transition of  $\text{Mn}^{2+}$  ions, decreased progressively as the  $\text{Mn}^{2+}$  ion doping concentration increased from 0.12% to 4.2% (Figure 4e). This decrease signifies the occurrence of energy transfer from the  $\text{K}_3\text{SbCl}_6$  host to  $\text{Mn}^{2+}$ .

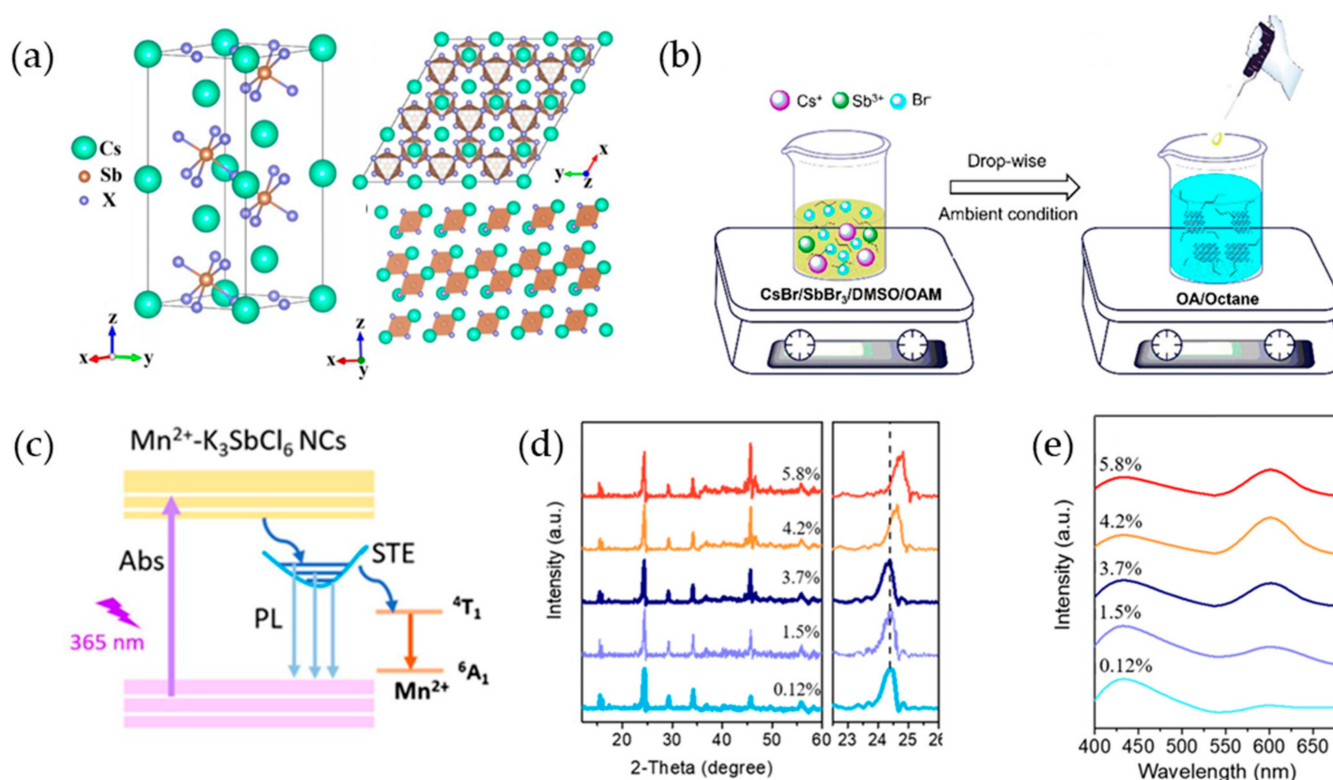


**Figure 4.** (a) Crystal structure of  $\text{Cs}_3\text{Sb}_2\text{X}_9$  ( $\text{X} = \text{Cl}$ ,  $\text{Br}$ , and  $\text{I}$ ), with a specific view of its  $xy$  plane illustrating the spatial distribution of  $\text{Cs}$ ,  $\text{Sb}$ , and  $\text{X}$  atoms within the crystal lattice and layered form; (a) reprinted with permission from Ref. [96]. Copyright 2022, MDPI. (b) Schematic image of the  $\text{Cs}_3\text{Sb}_2\text{Br}_9$  NC precursor reaction system for the ligand-assisted reprecipitation (LARP) technique; (b) reprinted with permission from Ref. [98]. Copyright 2017, American Chemical Society. (c) The PL mechanism of  $\text{Mn}^{2+}$ -doped  $\text{K}_3\text{SbCl}_6$  NCs; (d) XRD patterns of as-prepared  $\text{Mn}^{2+}$ -doped  $\text{K}_3\text{SbCl}_6$  NCs at different doping concentrations; (e) PL spectra of  $\text{Mn}^{2+}$ -doped  $\text{K}_3\text{SbCl}_6$  NCs at different doping concentrations under excitation at 365 nm; (c–e) Reprinted with permission from Ref. [99]. Copyright 2020, Elsevier.

Sb-PeNCs are environmentally friendly B-site substitutes and are capable of forming an  $A_3B(III)_2X_9$  structure by the heterovalent replacement of Pb cations. One of the advantages of this structure is the feasibility of low-temperature synthesis and greater thermodynamic stability compared with the 2D perovskite phase. However, the lack of a suitable synthesis method for producing high-quality Sb-PeNCs remains a limitation, leading to poor morphology and hindering their application. A doping strategy shows great potential for solid-state lighting applications but may require different approaches for high-purity displays.

#### 2.4. Cu-Based Perovskite Nanocrystals

Transition metals such as Cu have gained considerable attention because of their low toxicity, abundance, excellent stability, and high PLQYs compared to other transition metal-based MHPs [102–104]. The small ionic radius of Cu, measuring 0.77 nm for  $Cu^+$  and 0.73 nm for  $Cu^{2+}$ , prevents it from conforming to a tolerance factor of 1 and maintaining a 3D structure. Therefore, Cu mainly has electronic 0D or 1D structures, which have special optical properties owing to their large exciton binding energies, the  $A_xCu_yX_{x+y}$  structure in monovalent form, and the  $A_xCu_yX_{x+2y}$  structure in divalent form [102,105].

In the synthesis of Cu(II)-PeNCs, such as  $Cs_2CuX_4$ ,  $Cs_2CuI_4$  could not be obtained because pure Cu(II) diiodide is unstable and decomposes easily into iodine and Cu(I) iodide.  $Cs_2CuCl_4$  exhibited a broad PL spectral range of 400–650 nm, with a PLQY of 51.8%. Therefore, extensive research has focused on Cu (I)-PeNCs owing to the instability and broad emission spectra of Cu(II)-PeNCs [106].

Cu(I)-PeNCs exhibit structural variations depending on the A-site. When Cs is located at the A-site of Cu-PeNC,  $Cs_3Cu_2X_5$  and  $CsCu_2X_3$  structures are observed (Figure 5a) [107]. The space groups of the structures were identified from their XRD patterns (Figure 5b) [108].  $Cs_3Cu_2I_5$  belongs to the Pnma orthorhombic space group, and its crystal structure consists of  $[Cu_2I_5]^{3-}$  cluster units composed of tetrahedral  $[CuI_4]$  and trigonal planar  $[CuI_3]$  units that are separated from the  $Cs^+$  ions. This arrangement gives rise to an electronic 0D structure [109].  $CsCu_2I_3$  belongs to the Cmc space group of orthorhombic crystal systems and exhibits a 1D chain-like structure. This structure is formed by tetrahedral  $[CuI_4]^{3-}$  units that share a common edge, connecting them in a linear structure. By contrast, Cu(I)-PeNCs with Rb or K at the A-site follow the  $A_2CuX_3$  structure, which belongs to the Pnma space group. They exhibit a 1D shape where tetrahedral  $[CuX_4]^{3-}$  units share only the common vertex of the halides, resulting in a chain-like structure [110]. Overall, Cu(I)-PeNCs exhibit diverse crystal structures, including 0D and 1D forms, depending on the specific combination of the A-site and X-site compositions.

In the excited state, Cu-PeNCs show reorganization owing to the Jahn–Teller distortion that forms STE energy states and induces a Stokes shift, representing the difference between the absorption and emission spectra. In the case of  $Cs_3Cu_2X_5$ , the absorption of photon energy converts Cu(I)  $3d^{10}$  to Cu(II)  $3d^9$ , which changes the electronic configuration and induces a Jahn–Teller distortion (Figure 5c) [111]. Similarly, the conduction and valence bands of  $CsCu_2I_3$  are also dispersed along the direction parallel to the tetrahedral  $[Cu_2I_6]^{4-}$  chain, but when it is excited, the electrons are localized due to strong Coulombic coupling and large structural distortion of the  $[Cu_2I_6]^{4-}$  tetrahedron, and the structure is reorganized [112–114]. When the lattice distortion energy is high, charges are trapped because the trapped state is more stable than the strained state. Therefore, the Jahn–Teller distortion, which forms STE states, effectively confines charges to localized regions. Simultaneously, as STEs are formed, the ground state energy increases owing to the lattice strain energy. Consequently, STE emission exhibits a large Stokes shift [115,116]. The emission energy ( $E_{em}$ ) from the STE states can be expressed as follows [116]:

$$E_{em} = E_g - E_b - E_{st} - E_d \quad (3)$$

where  $E_g$ ,  $E_b$ ,  $E_{st}$ , and  $E_d$  represent the bandgap energy, the exciton binding energy, the self-trapping energy, and the lattice strain energy, respectively. The smaller distortion in

$\text{CsCu}_2\text{I}_3$  compared to the octahedral distortion in  $\text{Cs}_3\text{Cu}_2\text{I}_5$  indicates a smaller bandgap of  $\text{CsCu}_2\text{I}_3$  (Figure 5d,e) [117]. Moreover, the extended PL decay lifetime of the time-resolved photoluminescence (TrPL) in  $\text{Cs}_3\text{Cu}_2\text{I}_5$  compared to that in  $\text{CsCu}_2\text{I}_3$  can be attributed to two key factors: the augmented exciton binding energy and significant lattice distortion.  $\text{Cs}_3\text{Cu}_2\text{I}_5$  exhibits an enhanced exciton binding energy of 224 meV, while  $\text{CsCu}_2\text{I}_3$  has a relatively low binding energy of 123 meV. The higher exciton binding energy in  $\text{Cs}_3\text{Cu}_2\text{I}_5$  decelerates the exciton decay rate, resulting in an extended PL lifetime [118,119].

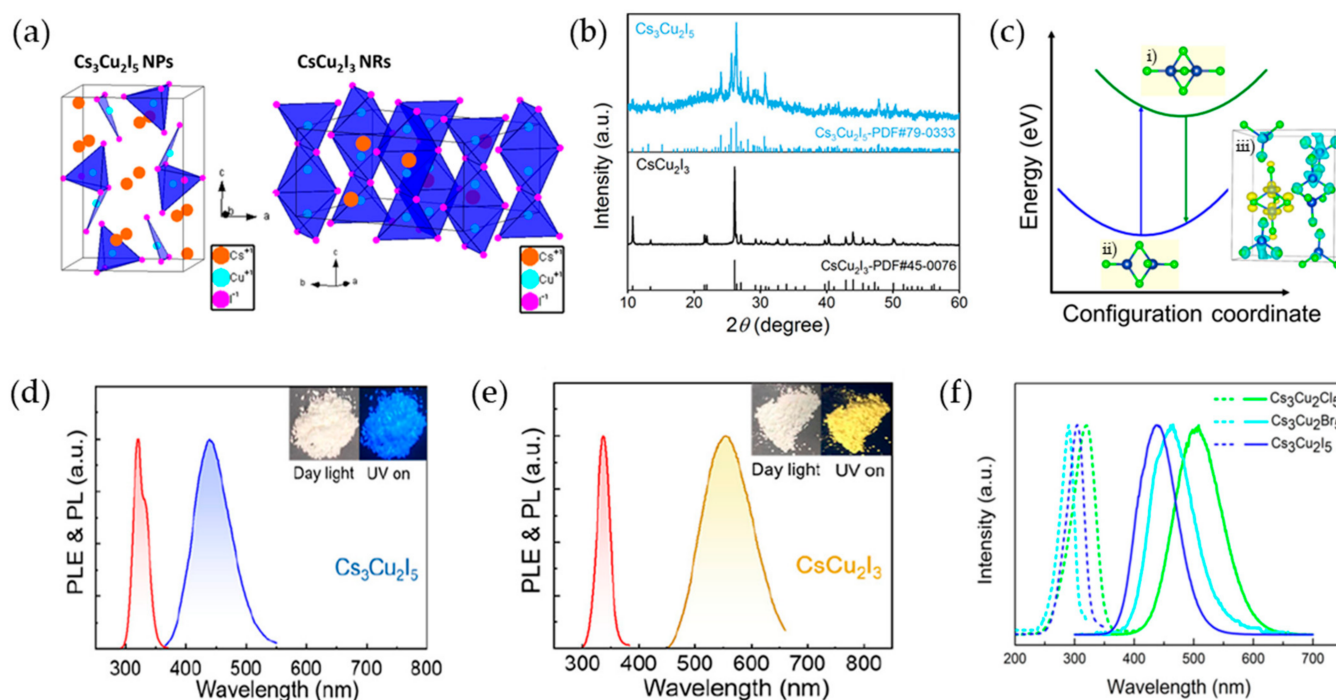


**Figure 5.** (a) Crystal structures of 0D  $\text{Cs}_3\text{Cu}_2\text{I}_5$  and 1D  $\text{CsCu}_2\text{I}_3$ ; (a) Reprinted with permission from Ref. [107]. Copyright 2019, American Chemical Society. (b) XRD patterns of  $\text{Cs}_3\text{Cu}_2\text{I}_5$  and  $\text{CsCu}_2\text{I}_3$ ; (b) reprinted with permission from Ref. [108]. Copyright 2022, American Chemical Society. (c) Schematic illustration of the principle of STE. (i) A self-trapped state; (ii) a ground state; (iii) charge density for conduction and valence bands; (d) PL and PLE spectra of  $\text{Cs}_3\text{Cu}_2\text{I}_5$ ; (e) PL and PLE spectra of  $\text{CsCu}_2\text{I}_3$ ; (d,e) Reprinted with permission from Ref. [117]. Copyright 2021, American Chemical Society (f) PLE (CI = 320 nm, Br = 290 nm, I = 305 nm) and PL (CI = 515 nm, Br = 461 nm, I = 445 nm) spectra of  $\text{Cs}_3\text{Cu}_2\text{X}_5$  at room temperature; (c,f) Reprinted with permission from Ref. [111]. Copyright 2020, American Chemical Society.

By tuning the halogen anions ( $\text{X} = \text{Cl}$ ,  $\text{Br}$ , and  $\text{I}$ ), the emission wavelength of  $\text{Cs}_3\text{Cu}_2\text{X}_5$  can be controlled, ranging from the green wavelength region (515 nm,  $\text{Cs}_3\text{Cu}_2\text{Cl}_5$ ) to the blue wavelength region (445 nm,  $\text{Cs}_3\text{Cu}_2\text{I}_5$ ) (Figure 5f) [111]. This spectral tunability of  $\text{Cs}_3\text{Cu}_2\text{X}_5$  is attributed to the effect of the halogen size and electronegativity on the electronic structure. During electron excitation, as the halogen radius increases and electronegativity decreases, stronger hybridization between the halogen  $p$ -orbital and the Cu  $3d$  orbital is induced [120,121]. This enhanced hybridization leads to a decrease in the valence band maximum (VBM) of  $\text{Cs}_3\text{Cu}_2\text{X}_5$ . Contrary to the general trend, this decrease in the VBM increases the band gap, leading to a blue shift in the emission wavelength. This phenomenon can be attributed to electronic interactions between the halogen and Cu atoms, which modulate the energy levels and affect the emission properties.

A hot-injection method was used to synthesize 0D  $\text{Cs}_3\text{Cu}_2\text{X}_5$  and 1D  $\text{CsCu}_2\text{X}_3$  by controlling the reaction temperature [118]. In this synthesis method, nucleation was induced within a short time by injecting a Cs-oleate into a Cu-oleate containing OAm and OA ligand molecules as quickly as possible and then cooling the solution. When the temperature



of Cu-oleate reached 70 °C and the Cs-oleate solution was rapidly injected, 0D Cs<sub>3</sub>Cu<sub>2</sub>I<sub>5</sub> NCs were synthesized, and when injected at a high temperature of 110 °C, 1D CsCu<sub>2</sub>I<sub>3</sub> was synthesized as the final product. The synthesized Cs<sub>3</sub>Cu<sub>2</sub>I<sub>5</sub> NCs exhibited blue PL at 441 nm and a PLQY of 67%, whereas the 1D CsCu<sub>2</sub>I<sub>3</sub> NCs exhibited yellow PL at 553 nm and a PLQY of ~5%.

Using an anti-solvent precipitation method, 0D Cs<sub>3</sub>Cu<sub>2</sub>X<sub>5</sub> and 1D CsCu<sub>2</sub>X<sub>3</sub> can also be synthesized by adjusting the concentration of the precursor solution and the amount of anti-solvent [122]. The CsI and CuI precursors were dissolved in a good solvent, such as DMF or DMSO, and then an anti-solvent such as ethanol was added to precipitate the Cu-PeNC. 1D CsCu<sub>2</sub>I<sub>3</sub> can be obtained in a low-concentration precursor solution because Cu<sup>+</sup> precipitates rapidly when an antisolvent is added to a low-concentration precursor. As the concentration of the precipitated Cu<sup>+</sup> ions increases, the number of ions participating in the crystallization process increases, and 1D CsCu<sub>2</sub>I<sub>3</sub> is synthesized. By contrast, 0D Cs<sub>3</sub>Cu<sub>2</sub>I<sub>5</sub> can be obtained from a high-concentration precursor solution (0.4 M) without a significant change in the Cs:Cu ratio when an antisolvent is added. The synthesized Cs<sub>3</sub>Cu<sub>2</sub>I<sub>5</sub> NCs exhibited a PL emission peak at 440 nm with a full width at half maximum (FWHM) of 73 nm and a PLQY of 67%, whereas 1D CsCu<sub>2</sub>I<sub>3</sub> exhibited a PL emission peak at 580 nm with a broad FWHM of 125 nm and a low PLQY of 7.4%.

During the hot-injection process, metal halide doping, such as with a ZnI<sub>2</sub> precursor, can lead to a surface passivation effect in Cs<sub>3</sub>Cu<sub>2</sub>X<sub>5</sub> NCs [123]. Additionally, Zn cation doping resulted in a tetrahedral coordination arrangement, and Cu<sup>+</sup> ions were heterosubstituted with Zn<sup>2+</sup> ions. This doping enriched the excited electron density, thereby enhancing the STE emission. Moreover, the incorporation of ZnI<sub>2</sub> results in enriched I anions, which can effectively reduce the number of non-radiative centers caused by the iodine vacancies. Zn-doped Cs<sub>3</sub>Cu<sub>2</sub>I<sub>5</sub> NCs exhibited a blue emission peak at ~440 nm with an FWHM of 73 nm. The PLQY increased from 72.2% for Cs<sub>3</sub>Cu<sub>2</sub>I<sub>5</sub> NCs to 92.8% for the Zn-doped Cs<sub>3</sub>Cu<sub>2</sub>I<sub>5</sub> NCs.

Cu-PeNCs can be synthesized in both the monovalent Cu<sup>+</sup> and divalent Cu<sup>2+</sup> forms using hot injection and antisolvent precipitation methods. In Cu(I)-PeNCs, lattice distortion arises from the structural characteristics of the PeNCs, resulting in STEs. This phenomenon contributes to a high PLQY and a prolonged PL lifetime resulting from highly localized electrons and holes. Moreover, in contrast to the typical red shift observed during the change in halide composition from Cl to I, the observed blue shift in the emission spectrum can be attributed to structural transformations and significant exciton effects. The emission wavelength and crystal structure can be controlled by adjusting the synthesis conditions, precursor ratios, and halide composition. Additionally, defect passivation can be facilitated through metal halide doping, which enhances the optical properties of the Cu-PeNCs. However, the broad FWHM of the emission spectrum stemming from the presence of STEs remains a major challenge to be solved using a novel approach in materials engineering.

## 2.5. Double Perovskite Nanocrystals

Pb-free double perovskites consist of two different cations occupying the B-sites of an A<sub>2</sub>BB'X<sub>6</sub> structure, providing high flexibility in the selection of B-site cations. The double perovskite structure maintains electrical neutrality by substituting two B<sup>2+</sup> ions with a B<sup>+</sup> cation and a B<sup>3+</sup> cation, forming an A<sub>2</sub>B(I)B(III)X<sub>6</sub> structure (Figure 6a, left). The B-site can accommodate monovalent cations such as K<sup>+</sup>, Na<sup>+</sup>, and Ag<sup>+</sup> and trivalent cations such as Bi<sup>3+</sup>, In<sup>3+</sup>, and Sb<sup>3+</sup>. Another structural variant is vacancy-ordered double perovskites, where two B<sup>2+</sup> ions are replaced by a single tetravalent cation, such as Sn<sup>4+</sup> or Ti<sup>4+</sup>, and B-site vacancies, forming the A<sub>2</sub>B(IV)X<sub>6</sub> structure (Figure 6a, right). Additionally, a 3D-layered structure with one vacancy can be achieved when four B<sup>2+</sup> ions are substituted by one B<sup>2+</sup> ion and two B<sup>3+</sup> ions, as represented by vacancy-ordered quadruple perovskites A<sub>4</sub>B(II)B(III)<sub>2</sub>X<sub>12</sub>. The incorporation of one Cu<sup>2+</sup> ion and two Sb<sup>3+</sup> ions in place of four Pb<sup>2+</sup> ions generates a single vacancy, resulting in the formation of a monoclinic layered



double perovskite structure such as  $\text{Cs}_4\text{CuSb}_2\text{Cl}_{12}$  (Figure 6b) [124]. Thus, the combination of B-site cations and vacancies results in a wide range of structural variations.

Double PeNCs have gained significant attention as promising candidates to replace Pb because of their tunable optoelectronic properties; high stability against heat, humidity, and light; and versatility in selecting B-site cations [125–128]. However, their commercial application is hindered by poor PL characteristics, which are attributed to intrinsic and surface defects, indirect bandgaps, and forbidden transitions [129–132]. To address these challenges, various strategies have been explored to improve their optoelectronic properties.

$\text{Ag}^+\text{Bi}^{3+}$ -PeNCs exhibit low PLQYs, mainly owing to their indirect bandgap characteristics [126,129,133]. The absorption tail observed in the long-wavelength region of the absorption spectrum indicates sub-bandgap absorption [70,132]. Yang et al. introduced changes in the indirect bandgap characteristics by doping  $\text{In}^{3+}$  ions in  $\text{Cs}_2\text{AgBiCl}_6$  NCs [134]. Optical analysis of the  $\text{Cs}_2\text{AgIn}_x\text{Bi}_{1-x}\text{Cl}_6$  NCs revealed blue-shifted absorption peaks with increasing  $\text{In}^{3+}$  doping concentration, and sharp absorption peaks were observed at  $x$  values of 0.75 and 0.9, indicating possible direct bandgap characteristics. The intensity of the PL emission peak observed at  $\sim 400$  nm increased with increasing  $\text{In}^{3+}$  doping concentration, and a second peak appeared at  $\sim 570$  nm at  $x > 0.75$ .

To gain a deeper understanding of the optical mechanism and bandgap characteristics, DFT calculations were performed using the generalized gradient approximation of the Perdew–Burke–Ernzerhof functional. Figure 6c,d depict the band structures of  $\text{Cs}_2\text{AgIn}_x\text{Bi}_{1-x}\text{Cl}_6$  NCs with In ratios of 0% and 75%, respectively. The band structure of  $\text{Cs}_2\text{AgBiCl}_6$  NC exhibits an indirect bandgap, whereas that of  $\text{Cs}_2\text{AgIn}_{0.75}\text{Bi}_{0.25}\text{Cl}_6$  NC shows a nearly direct bandgap. In the  $\text{Cs}_2\text{AgBiCl}_6$  NC, the VBM at the  $\Gamma$  point has Cl- $p$ , Ag- $d$ , and Bi- $s$  characteristics, whereas the CBM at L has Bi- $p$ , Cl- $p$ , and Ag- $s$  characteristics. Conversely, in the  $\text{Cs}_2\text{AgIn}_{0.75}\text{Bi}_{0.25}\text{Cl}_6$  NC, the VBM at the  $\Gamma$  point has Cl- $p$ , Ag- $d$ , and Bi- $s$  characteristics, similar to those of the  $\text{Cs}_2\text{AgBiCl}_6$  NC, whereas the CBM comprises In- $s$ , Cl- $p$ , and Ag- $s$  characteristics, similar to those of the  $\text{Cs}_2\text{AgInCl}_6$  NC. This indicates the possibility of direct transitions, as observed in the band structure of the  $\text{Cs}_2\text{AgIn}_{0.75}\text{Bi}_{0.25}\text{Cl}_6$  NC. Similar to  $\text{Cs}_2\text{AgInCl}_6$  NC, where a parity-forbidden transition from the VBM to the CBM occurs at the  $\Gamma$  point,  $\text{Cs}_2\text{AgIn}_{0.75}\text{Bi}_{0.25}\text{Cl}_6$  NC provides a pathway for relaxation through parity-forbidden transitions, leading to emission at approximately 570 nm [135]. These results suggest that the dual PL emission peaks can be attributed to the emissions resulting from both band- and parity-forbidden transitions. The PLQYs showed a pronounced enhancement above 0.75 in the doping ratio, resulting in a PLQY of 36.6% in  $\text{Cs}_2\text{AgIn}_{0.75}\text{Bi}_{0.25}\text{Cl}_6$  NC, but a slight increase below 0.5 in the doping ratio, resulting in a PLQY of  $\sim 10\%$  in  $\text{Cs}_2\text{AgIn}_{0.5}\text{Bi}_{0.5}\text{Cl}_6$  NC. This substantial improvement in the PLQY above 0.75 in the ratio originates from the transition from an indirect bandgap to a direct bandgap (Figure 6e). Band structure diagrams in Figure 6f,g depict the photoinduced charge carrier transportation mechanism and provide an intuitive understanding of the absorption and emission processes based on the indirect and direct bandgap characteristics of the double PeNCs. In the case of an indirect bandgap, both direct and indirect transitions can occur. These indirect bandgap transitions require phonon participation, resulting in a low PLQY [136,137]. However, for a direct bandgap, absorption occurs through direct transitions, and the excited carriers can undergo non-radiative relaxation processes to the forbidden states, resulting in two forms of luminescence: direct bandgap relaxation and relaxation to the forbidden states. Radiative relaxation of the band edge and forbidden states improved the PLQY of  $\text{Cs}_2\text{AgIn}_x\text{Bi}_{1-x}\text{Cl}_6$  when  $x$  was greater than 0.75.

$\text{Cs}_2\text{SnX}_6$ -based vacancy-ordered double perovskites utilizing  $\text{Sn}^{4+}$  have attracted significant research interest owing to their air and moisture stability, high absorption coefficients, and carrier mobility [138–140]. Wang et al. reported a synthesis method for  $\text{Cs}_2\text{SnI}_6$  perovskites that could be adjusted from spherical NCs, nanorods, nanowires, and nanobelts to nanoplatelets by varying the reaction time during the hot-injection process [141]. However, the PLQY of the  $\text{Cs}_2\text{SnI}_6$  NCs was found to be as low as 0.48%.  $\text{Cs}_2\text{SnI}_6$  NCs can also

be synthesized by a ligand-mediated approach using the hot-injection method, similar to conventional LHP NC synthesis [142–144]. By adjusting the ratio of OA to octylamine, the structure of the  $\text{Cs}_2\text{SnI}_6$  NCs could be controlled between the 3D and 2D forms. When only OA was used during the synthesis, 3D  $\text{Cs}_2\text{SnI}_6$  NCs were formed, whereas the combination of OA and octylamine resulted in the formation of 2D  $\text{Cs}_2\text{SnI}_6$  nanoplatelets. The one-layer 2D  $\text{Cs}_2\text{SnI}_6$  exhibited a PL emission peak at 643 nm, while the two-layer 2D  $\text{Cs}_2\text{SnI}_6$  displayed a PL emission peak at 742 nm. The PLQYs were measured as 28% for the one-layer  $\text{Cs}_2\text{SnI}_6$  and 16% for the two-layer  $\text{Cs}_2\text{SnI}_6$ . These results can be attributed to the quantum confinement effect of the quantum-well structure, which enhances the exciton binding energy and improves the PL characteristics [145,146].

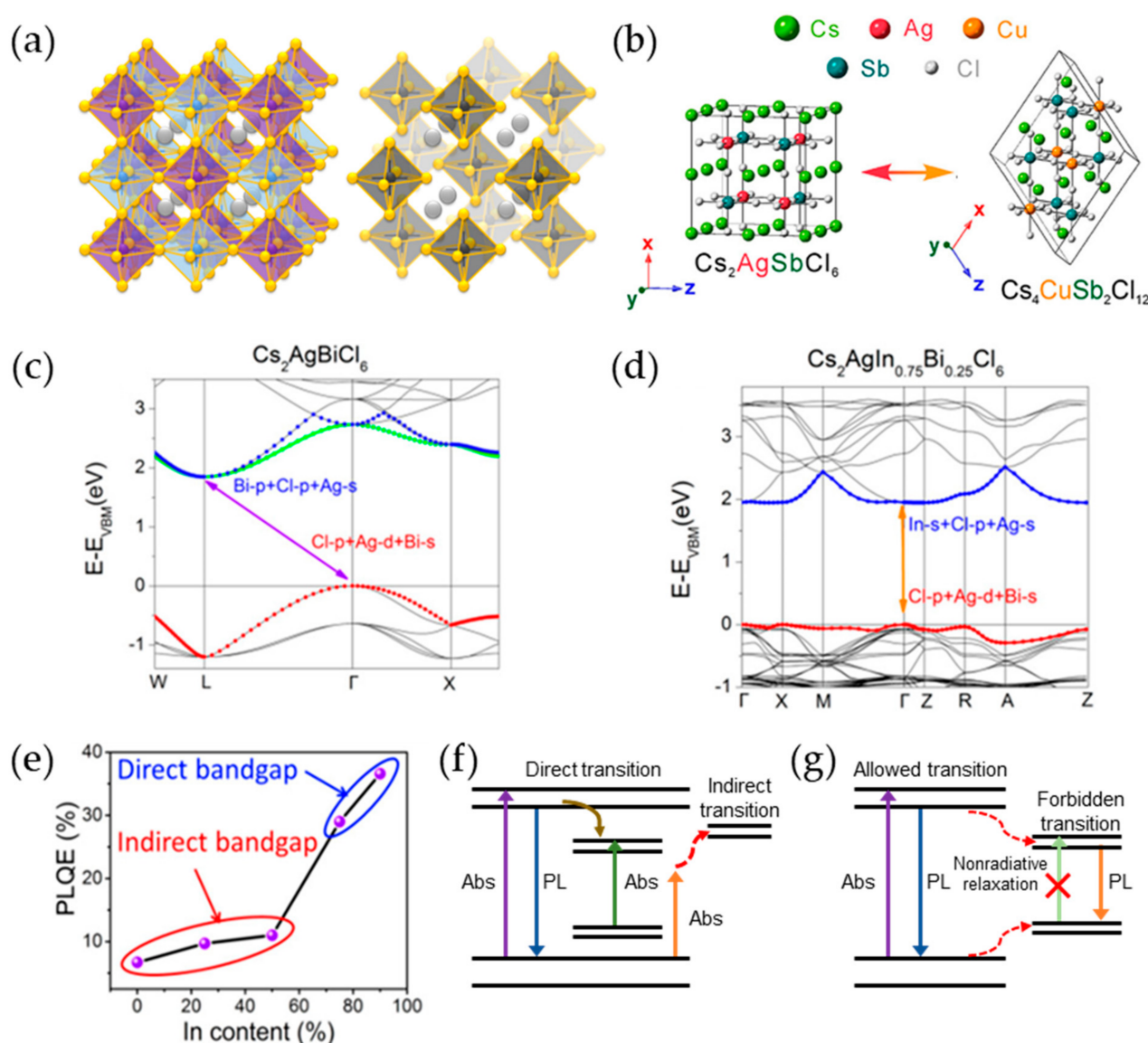


**Figure 6.** (a) Crystal structures of double perovskites ( $\text{A}_2\text{B(IV)X}_6$ ) and vacancy-ordered double perovskites ( $\text{A}_2\text{B(III)X}_6$ ); (b) crystal structures of  $\text{Cs}_4\text{Cu(II)Sb(III)}_2\text{Cl}_{12}$  and  $\text{Cs}_2\text{Ag(I)Sb(III)Cl}_6$ ; (b) reprinted with permission from Ref. [124]. Copyright 2020, American Chemical Society. Band structures of (c)  $\text{Cs}_2\text{AgBiCl}_6$  and (d)  $\text{Cs}_2\text{AgIn}_{0.75}\text{Bi}_{0.25}\text{Cl}_6$ ; (e) PLQE value of  $\text{Cs}_2\text{AgIn}_x\text{Bi}_{1-x}\text{Cl}_6$  (x = 0, 0.25, 0.5, 0.75, and 0.9) NCs; (c–e) reprinted with permission from Ref. [134]. Copyright 2018, American Chemical Society. Charge carrier transportation mechanism models of (f) indirect bandgap  $\text{Cs}_2\text{AgIn}_x\text{Bi}_{1-x}\text{Cl}_6$  NCs and (g) direct bandgap  $\text{Cs}_2\text{AgIn}_x\text{Bi}_{1-x}\text{Cl}_6$  NCs.

Similar to the behavior of other PeNCs, doping of metal ions, such as  $\text{Sb}^{3+}$ , in  $\text{Cs}_2\text{SnCl}_6$  NCs is an effective strategy for enhancing their luminescent properties [147]. Pristine  $\text{Cs}_2\text{SnCl}_6$  NCs synthesized by the hot-injection process exhibited a sharp absorption edge at 310 nm with an absorption tail at longer wavelengths (Figure 7a). Under 365 nm excitation, the pristine  $\text{Cs}_2\text{SnCl}_6$  NCs showed a PL spectrum peak at 438 nm with a PLQY of 4.37%.  $\text{Sb}^{3+}$  doping of the  $\text{Cs}_2\text{SnCl}_6$  NCs was achieved with Sb/Sn precursor ratios of 0.05 and 0.1, where  $\text{SbCl}_3$  was mixed concurrently with  $\text{SnCl}_2$ . The  $\text{Sb}^{3+}$ -doped  $\text{Cs}_2\text{SnCl}_6$  NCs exhibited double PL peaks at 438 and 615 nm, and the PL intensity at 615 nm increased with increasing  $\text{Sb}^{3+}$  concentration from 0.05 to 0.1 (Figure 7b). Further investigations revealed that the 615 nm emission could be attributed to the triplet states of STE induced by  $\text{Sb}^{3+}$  doping. The emission at 615 nm originates from recombination with the ground states through transitions from the singlet states of STE with emission at  $\sim 450$  nm to the triplet states of STE with emission at 615 nm, resulting in broad emission wavelengths. Through  $\text{Sb}^{3+}$  doping at a ratio of 0.1, the PLQY of  $\text{Sb}^{3+}$ -doped  $\text{Cs}_2\text{SnCl}_6$  was enhanced to 8.25% compared to that of pristine  $\text{Cs}_2\text{SnCl}_6$  (4.37%).

Vacancy-ordered quadruple perovskite  $\text{A}_4\text{B(II)B(III)}_2\text{X}_{12}$  has attracted significant research interest because of its large compositional space, direct bandgap characteristics, and excellent structural stability [148–151]. It consists of  $[\text{M(II)X}_6]^{4-}$  octahedra layers sandwiched between  $[\text{M(III)X}_6]^{3-}$  octahedra layers, crystallizing in the  $R\bar{3}m$  space group symmetry perpendicular to the  $\langle 111 \rangle$  direction of the cubic perovskite structure. However, their practical applications have been hindered by their poor luminescence properties. Therefore, research has focused on enhancing the luminescent characteristics of vacancy-ordered quadruple perovskites through metal cation doping [124,152–157]. The synthesis of  $\text{Cs}_4\text{Cd}_{1-x}\text{Mn}_x\text{Bi}_2\text{Cl}_{12}$  NCs was proposed using a hot-injection method with benzoyl chloride [152]. The  $[\text{Mn}]/([\text{Mn}] + [\text{Cd}])$  ratios in the final products were quantified as 0%, 1.7%, 10.1%, 34.9%, 69.0%, and 100% using inductively coupled plasma atomic emission spectroscopy. Despite an increase in the Mn ratio, the absorption and PLE spectra showed minimal changes, whereas there was a distinct red shift in the PL emission spectra (Figure 7c). The  $\text{Cs}_4\text{Cd}_{1-x}\text{Mn}_x\text{Bi}_2\text{Cl}_{12}$  NCs with  $x = 0.349$  exhibit the highest PLQY of 4.6%. However, as the value of  $x$  increased further, the PLQY decreased. In Figure 7c, the Stokes shift originated from a difference between absorption and emission peaks. The influences of Stokes shift and self-absorption in PeLEDs have been commonly explained in two ways. First, self-absorption can cause photon loss due to a difference between the numbers of internally generated and externally emitted photons that can be measured as PLQYs [158]. However, the large Stokes shift could prevent self-absorption loss because the absorption spectrum does not overlap with the emission wavelength. Therefore, reduced self-absorption resulting from the Stokes shift could enhance emission efficiencies in LEDs. Secondly, however, the Stokes shift could be observed along with the increase in Auger recombination affected by the large exciton binding energy, which can lead to increased efficiency roll-off in LEDs [159–161]. Therefore, further systematic analysis should be studied to clearly establish the effects of the Stokes shift on LED performance.

Similar PL characteristics were observed for  $\text{Cs}_4\text{Cd}_{1-x}\text{Mn}_x\text{Bi}_2\text{Cl}_{12}$  nanosheets (NS) with the same constituent elements. Bhardwaj et al. synthesized  $\text{Cs}_4\text{Cd}_{0.6}\text{Mn}_{0.4}\text{Bi}_2\text{Cl}_{12}$  and 2- to 3-layer-thick 2D NS [157]. Optical characterization of pristine  $\text{Cs}_4\text{CdBi}_2\text{Cl}_{12}$  and  $\text{Cs}_4\text{Cd}_{0.6}\text{Mn}_{0.4}\text{Bi}_2\text{Cl}_{12}$  NS revealed that a weak PL emission appeared at  $\sim 605$  nm for the pristine  $\text{Cs}_4\text{CdBi}_2\text{Cl}_{12}$  NS, whereas the  $\text{Cs}_4\text{Cd}_{0.6}\text{Mn}_{0.4}\text{Bi}_2\text{Cl}_{12}$  NS showed a gradual increase in the PL emission peak intensity at  $\sim 601$  nm with increasing Mn doping concentration, unaffected by different excitation wavelengths (Figure 7d). These red-shifted PL spectra due to Mn doping were attributed to an inter-Mn-distance-induced Mn–Mn coupling interaction, leading to a larger  $d$ – $d$  splitting of the  $\text{Mn}^{2+}$  ion centers, consequently reducing the gap in the  ${}^4\text{T}_1$ – ${}^6\text{A}_1$  electronic transition of  $\text{Mn}^{2+}$  ions [152,162,163]. In  $\text{Cs}_4\text{CdBi}_2\text{Cl}_{12}$ , the emission arises from the STE state, whereas the emission in  $\text{Cs}_4\text{Cd}_{1-x}\text{Mn}_x\text{Bi}_2\text{Cl}_{12}$  arises from energy transfer to  $\text{Mn}^{2+}$  in the STE states [153].

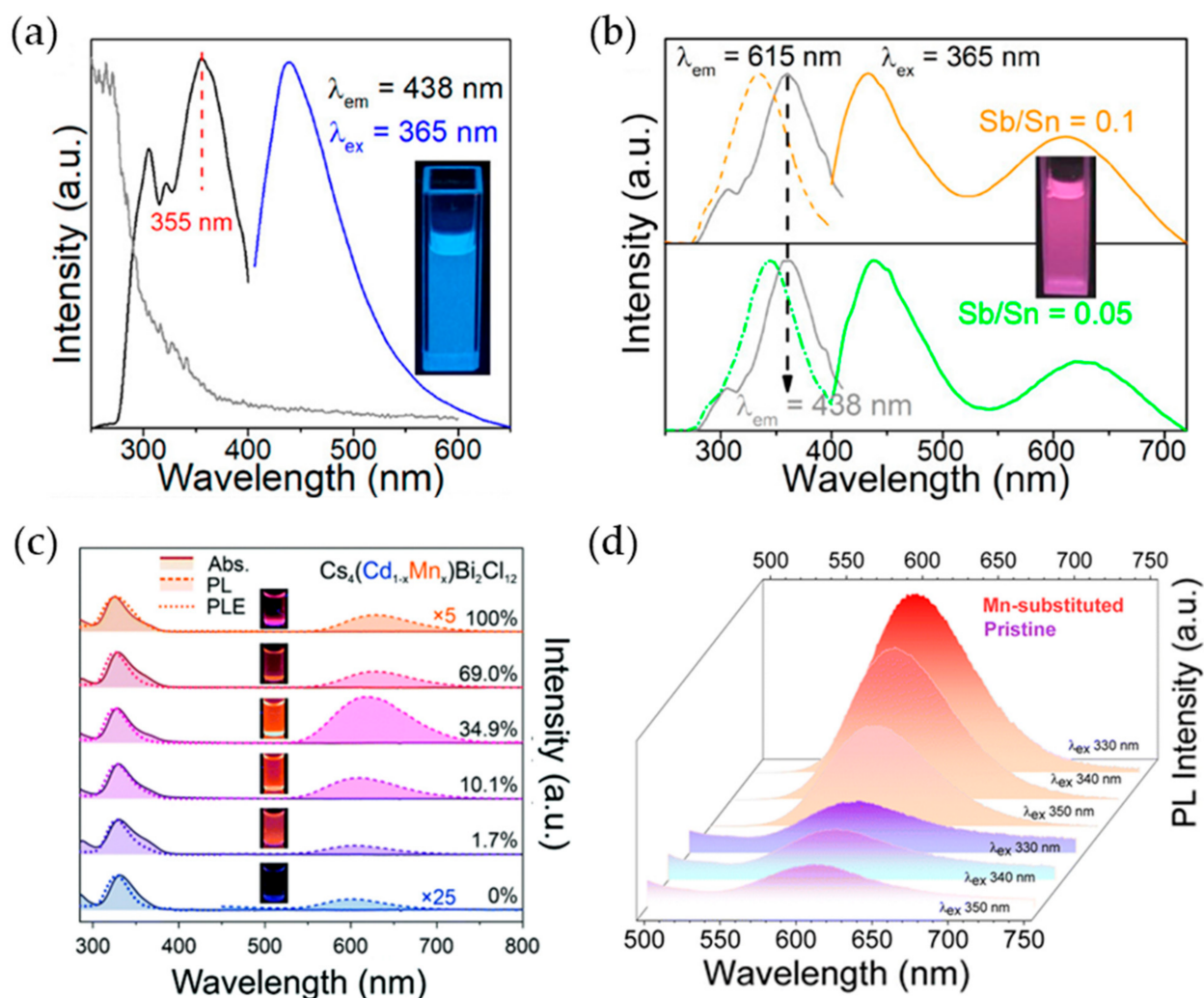


**Figure 7.** (a) Absorption (gray line) excitation (dashed line, emission at 438 nm) and PL (excitation at 365 nm) spectra of undoped  $\text{Cs}_2\text{SnCl}_6$  NCs (inset: UV irradiation under 365 nm UV lamp); (b) PLE (dashed line, emission at 615 nm; gray line, emission at 438 nm) and PL (excitation at 365 nm) spectra of Sb-doped  $\text{Cs}_2\text{SnCl}_6$  NCs (inset: UV irradiation of Sb/Sn = 0.1 NCs under 365 nm UV lamp); (a,b) reprinted with permission from Ref. [147]. Copyright 2019, American Chemical Society. (c) Absorption, PLE, and PL spectra of  $\text{Cs}_4\text{Cd}_{1-x}\text{Mn}_x\text{Cl}_{12}$  NCs (inset: UV irradiation under UV light); (c) reprinted with permission from Ref. [152]. Copyright 2020, Royal Society of Chemistry. (d) Room temperature PL spectra of  $\text{Cs}_4\text{CdBi}_2\text{Cl}_{12}$  (pristine) and  $\text{Cs}_4\text{Cd}_{0.6}\text{Mn}_{0.4}\text{Bi}_2\text{Cl}_{12}$  (Mn-substituted) nanosheet (NS); (d) reprinted with permission from Ref. [157]. Copyright 2023, Royal Society of Chemistry.

Double PeNCs also have limitations in practical applications owing to issues concerning instability due to metal ion oxidation, the formation of deep trap states, and a broad FWHM of the emission spectrum. To overcome these issues, ongoing research aims to enhance the photoelectric performance of double PeNCs through various doping strategies, synthesis methods, and control of variables such as ligands [164–182]. The characterization of changes induced by process variables will lead to diverse applications in various optoelectronic fields.

Based on the above discussion, the optical and photophysical properties of the diverse PeNCs are summarized in Table 1. It is worth noting that certain instances of Pb-free PeNCs exhibit superior PL properties in comparison to LHP NCs. In particular, for remarkable PLQYs of Cu-based PeNCs, it could be necessary to focus on mainly developing device



engineering such as device physics, light out-coupling, and charge balance as future promising eco-friendly LEDs. On the other hand, for relatively low PLQYs of Sn-, Bi-, and double PeNCs, research on further developing their intrinsic material properties might be more crucial and would be helpful to further enhance PL properties through promising strategies such as defect passivation, ligand modification, surface engineering, and improved synthesis techniques.

**Table 1.** Optical and photophysical properties of PeNCs.

Perovskite	Absorption Peak (nm)	PL Peak (nm)	Stokes Shift (nm)	PLQY (%)	PL Lifetime (ns)	Reference
CsPbCl <sub>3</sub>	-	408	-	65	7.63	[24]
CsPbBr <sub>3</sub>	-	512	-	92	12.52	[24]
CsPbI <sub>3</sub>	-	691	-	58	20.99	[24]
FAPbBr <sub>3</sub>	-	545	28	-	18.7	[25]
CsPb(Br/I) <sub>3</sub> NC film	-	~650	-	15	26.2	[32]
CsSnBr <sub>3</sub> nanocages	655	685	30	2.1	6.52	[59]
PFOA-CsSnBr <sub>3</sub> nanocages	-	683	-	1.8	0.25	[59]
OA/OAm-CsSnCl <sub>3</sub>	~300	~440	~140	-	7.33	[61]
Gelatin-CsSnCl <sub>3</sub>	303	442	139	-	8.84	[61]
Cs <sub>3</sub> Bi <sub>2</sub> Br <sub>9</sub>	439	460	21	4.5	~2.7	[70]
Cl-MA <sub>3</sub> Bi <sub>2</sub> Br <sub>9</sub>	388	422	34	54.1	2.17	[95]
Cs <sub>3</sub> Sb <sub>2</sub> Br <sub>9</sub>	375	410	35	46	4.285	[97]
K <sub>3</sub> SbCl <sub>6</sub>	~328	440	120	22.3	535.2	[99]
K <sub>3</sub> SbCl <sub>6</sub> :Mn <sup>2+</sup>	318~320	600	280	37.2	3.2 × 10 <sup>6</sup>	[99]
CsCu <sub>2</sub> I <sub>3</sub>	321	561	240	11	0.1 × 10 <sup>3</sup>	[107]
Cs <sub>3</sub> Cu <sub>2</sub> I <sub>5</sub>	300	440	158	72.2	2.8 × 10 <sup>3</sup>	[122]
Cs <sub>3</sub> Cu <sub>2</sub> I <sub>5</sub> :InI <sub>3</sub>	295	440	145	96.6	1491	[102]
Cs <sub>2</sub> CuCl <sub>4</sub>	~300	388	88	51.8	-	[106]
Cs <sub>2</sub> CuBr <sub>4</sub>	360	393	33	37.5	-	[106]
Cs <sub>2</sub> AgBiBr <sub>6</sub>	500	625	125	-	7.5	[128]
Cs <sub>2</sub> AgBiCl <sub>6</sub>	~360	395	~35	6.7	-	[132]
Cs <sub>2</sub> SnCl <sub>6</sub>	317	438	121	4.37	11	[147]
Cs <sub>4</sub> CdBi <sub>2</sub> Cl <sub>12</sub>	331	~602	~271	<0.1	-	[152]

### 3. Pb-Free Perovskite Nanocrystal-Based LEDs

Pb-free perovskite LEDs (PeLEDs) exhibit great potential as next-generation LEDs. This is due to their nontoxicity, cost-effectiveness, solution processability, facile emission wavelength tunability, and defect tolerance. Research on colloidal PeNC-based LEDs has recently gained attention in parallel with the rapid advancement of solution-based synthesis of bulk MHPs [183–189]. Optimizing the dimensionality of MHPs provides another avenue for tuning their electronic and optical properties [190–192]. PeNCs possess distinct electrical and optical properties attributable to their large exciton binding energy, tunable NC size, and reduced dimensionality [19,193].

Most Sn-based MHPs are solution-processed for fabricating LEDs because of their simplicity and low-cost processability. However, the rapid crystallization of Sn-MHPs can lead to poor morphology and low film quality, which degrades the performance of



LEDs [194–196]. To overcome the intrinsic limitations of Sn-based PeLEDs, high-vacuum vapor deposition is an alternative approach for the fabrication of Sn-PeNC films [197,198]. The fabrication of PeLEDs based on  $\text{CsSnBr}_3$  PeNCs can be achieved by thermal evaporation with in-situ annealing [199]. To promote the formation of  $\text{CsSnBr}_3$  NCs films, a dual source was used for the thermal evaporation of CsBr and  $\text{SnBr}_2$ . Subsequently, in the post-synthetic annealing stage, the initially stacked CsBr and  $\text{SnBr}_2$  layers interact at the interface, resulting in the formation of a  $\text{CsSnBr}_3$  layer through interdiffusion of the constituent elements facilitated by thermal annealing [183]. When testing various post-synthetic annealing temperatures, the  $\text{CsSnBr}_3$  films annealed at 85 °C showed a significant enhancement in crystallinity. This is evident from the increased diffraction intensity of the (100) and (200) planes and a reduced FWHM. The improved crystallinity can be attributed to an enhanced reaction between the CsBr and  $\text{SnBr}_2$  precursors, which occurs as a result of interdiffusion. In addition, the  $\text{CsSnBr}_3$  NCs obtained by the annealing-temperature process exhibited an average crystal size of 39.9 nm. The devices were fabricated using the structure of ITO/ $\text{MoO}_3$ /4,4'-cyclohexylidenebis[N,N-bis(p-tolyl)aniline]/tris(4-carbazoyl-9-ylphenyl)amine (TCTA)/ $\text{CsSnBr}_3$  NCs/1,3,5-tri(m-pyrid-3-yl-phenyl)benzene (TmPyPB)/LiF/Al (Figure 8a). The  $\text{CsSnBr}_3$  NC-based LED demonstrated a turn-on voltage of 5.5 V (at 1 cd/m<sup>2</sup>) and a maximum luminance of 43 cd/m<sup>2</sup> at an applied voltage of 10 V. Notably, it achieved a high current efficiency (CE) of 0.34 cd/A and an external quantum efficiency (EQE) of 0.16% (Figure 8b). At an applied voltage from 4.5 to 10 V, the  $\text{CsSnBr}_3$  NC-based LED exhibited consistent electroluminescence (EL) emission peaks at approximately 675 nm, indicating exceptional EL stability.

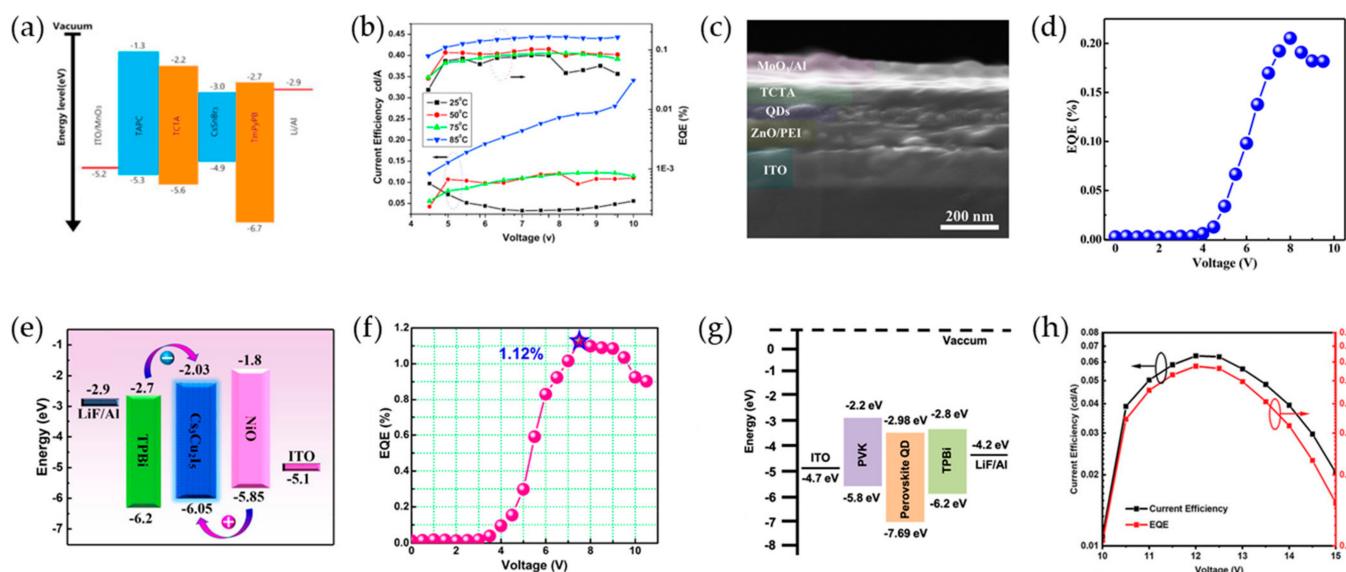


**Figure 8.** (a) Energy diagram of the PeLED with  $\text{CsSnBr}_3$  PeNCs; (b) current efficiency (CE) and external quantum efficiency (EQE) versus voltage curves of the  $\text{CsSnBr}_3$  NC-based PeLED at various in-situ annealing temperatures; (a,b) Reprinted with permission from Ref. [183]. Copyright 2020, Elsevier. (c) Cross-sectional scanning electron microscopy (SEM) image of ITO/ZnO nanoparticles (NP)/PEI/ $\text{Cs}_3\text{Sb}_2\text{Br}_9$  NCs/TCTA/ $\text{MoO}_3$ /Al; (d) EQE-voltage curve of  $\text{Cs}_3\text{Sb}_2\text{Br}_9$  NC-based PeLED; (c,d) reprinted with permission from Ref. [186]. Copyright 2020, American Chemical Society. (e) Energy band of the  $\text{Cs}_3\text{Cu}_2\text{I}_5$  NC-based LED; (f) EQE-voltage curve of  $\text{Cs}_3\text{Cu}_2\text{I}_5$  NCs PeLED; (e,f) reprinted with permission from Ref. [187]. Copyright 2020, American Chemical Society. (g) Energy band diagram of  $\text{Cs}_2\text{AgIn}_{0.9}\text{Bi}_{0.1}\text{Cl}_6$  NC-based PeLED; (h) current efficiency-voltage curve (black line) and EQE-Voltage curve of  $\text{Cs}_2\text{AgIn}_{0.9}\text{Bi}_{0.1}\text{Cl}_6$  NC-based PeLED; (g,h) reprinted with permission from Ref. [188]. Copyright 2021, Wiley-VCH.

Bi-based PeNC LEDs have not been reported yet. This may be caused by the low PLQY resulting from surface defects, which are due to the intrinsic self-trapping-induced phonon-mediated nonradiative process [93,95]. It could also be attributed to strong photon-phonon coupling and dangling bonds present on the PeNC surfaces [70,93,94]. As there are no reports on Bi-based PeNCs LED yet, further research is necessary to improve PLQY and engineering for LED applications.

$\text{Sb}^{3+}$ , possessing an electronegativity similar to that of  $\text{Pb}^{2+}$  ions, demonstrates exceptional structural stability and outstanding luminescent properties, making it a promising candidate for incorporation as an emitting layer (EML) in LEDs. Stable violet-emitting  $\text{Cs}_3\text{Sb}_2\text{Br}_9$  NCs, synthesized using the LARP method, exhibited a high PLQY of 51.2% [186]. Moreover, the  $\text{Cs}_3\text{Sb}_2\text{Br}_9$  NCs exhibited a moderate PL stability change of  $\sim 17.5\%$  after 73 h of continuous UV irradiation (365 nm, 30 W). Furthermore, the PL intensity of the  $\text{Cs}_3\text{Sb}_2\text{Br}_9$  NCs was maintained at approximately 80% of the initial emission intensity when 0.5 mL of deionized water was added to the  $\text{Cs}_3\text{Sb}_2\text{Br}_9$  NC solution for 45 h, while the  $\text{CsPbBr}_3$  NCs experienced rapid fluorescence quenching, retaining only  $\sim 9\%$  of the initial emission intensity for only 4 h. Moreover, the fabricated PeLED with the structure ITO/ZnO/PEI/ $\text{Cs}_3\text{Sb}_2\text{Br}_9$  NCs/TCTA/MoO<sub>3</sub>/Al exhibited a maximum EQE of  $\sim 0.206\%$  and luminance of 29.6 cd/m<sup>2</sup> at an operating voltage of 8.0 V (Figure 8c,d). The EL intensity peak was maintained at a wavelength of 408 nm after 6 h of device operation, and the PeLED demonstrated excellent operational EL stability, with only  $\sim 10\%$  emission decay.

Cu-based PeLEDs are attracting attention as blue-light emitters owing to their non-toxicity, high stability, and excellent optoelectronic properties. Wang et al. reported a Cu(I)-based PeLED with the structure ITO/NiO/ $\text{Cs}_3\text{Cu}_2\text{I}_5$  NCs/2,2',2''-(1,3,5-Benzinetriyl)-tris(1-phenyl-1-H-benzimidazole) (TPBi)/LiF/Al [187].  $\text{Cs}_3\text{Cu}_2\text{I}_5$  NCs synthesized by the hot-injection method were employed as an EML fabricated by the spin-coating process. The energy band diagram of ITO/NiO/ $\text{Cs}_3\text{Cu}_2\text{I}_5$  NCs/TPBi/LiF/Al was obtained using ultraviolet photoelectron spectroscopy (UPS) (Figure 8e). The device structure illustrates that p-NiO possesses a relatively high ionization potential energy, making it a suitable hole-donating and electron-blocking layer because of its compatible electron affinity with the  $\text{Cs}_3\text{Cu}_2\text{I}_5$  NCs [200]. Similarly, TPBi served the dual function of electron donation and a hole-blocking layer owing to its low, lowest unoccupied molecular orbital and highest occupied molecular orbital energy levels. Electrons were injected from the upper TPBi layer into the  $\text{Cs}_3\text{Cu}_2\text{I}_5$  NC EML, facilitating EL emission through the recombination of confined electrons and holes.

$\text{Cs}_3\text{Cu}_2\text{I}_5$  NC-LED exhibited a Commission International de l'Eclairage (CIE) coordinate of (0.16, 0.07) at 7.0 V, in compliance with the blue coordinate of the National Television Standards Committee (NTSC) standard, reaching  $\sim 99\%$  of the NTSC standard and contributing to a wide color gamut for Pb-free PeLEDs. Additionally, the maximum EQE of the  $\text{Cs}_3\text{Cu}_2\text{I}_5$  NC-LEDs was  $\sim 1.12\%$  (Figure 8f), with high reproducibility and a small relative deviation of 15.7%. Furthermore,  $\text{Cs}_3\text{Cu}_2\text{I}_5$  NC-LED demonstrated continuous, relatively stable device operation for 170 h at an applied voltage of 6.7 V while maintaining an EL wavelength of 445 nm. These results indicate the excellent device performance and operational stability of  $\text{Cs}_3\text{Cu}_2\text{I}_5$  NC-LEDs.

Double PeNCs face challenges in LED implementation, owing to their intrinsic and surface defects, indirect bandgaps, and suppressed emission characteristics [129–132]. However, attempts have been made to improve the optical properties of LED implementation through bandgap modification by metal cation doping and changes in carrier dynamics. Zhang et al. first developed electrically excited white LEDs based on  $\text{Cs}_2\text{AgIn}_{0.9}\text{Bi}_{0.1}\text{Cl}_6$  NCs without a phosphor [188].  $\text{Cs}_2\text{AgIn}_{0.9}\text{Bi}_{0.1}\text{Cl}_6$  NCs were synthesized using a hot-injection method with TMS-Cl injection. The  $\text{Cs}_2\text{AgIn}_{0.9}\text{Bi}_{0.1}\text{Cl}_6$  NCs exhibited two absorption peaks at 333 and 367 nm, a broad dual-color emission from STE emission, and a PLQY of 31.4%. The energy band structure of  $\text{Cs}_2\text{AgIn}_{0.9}\text{Bi}_{0.1}\text{Cl}_6$  NCs was determined by UPS measurements, revealing a CBM of  $-7.69$  eV and a VBM of  $-2.98$  eV obtained by a Tauc plot.

DFT calculations demonstrated a direct bandgap for  $\text{Cs}_2\text{AgIn}_{0.9}\text{Bi}_{0.1}\text{Cl}_6$ , and band symmetry analysis indicated that the parity-forbidden transition is broken at the deep-energy level of the conduction band because of the contribution of the Bi atom [135]. A device was fabricated with the structure ITO/Poly(9-vinylcarbazole) (PVK)/ $\text{Cs}_2\text{AgIn}_{0.9}\text{Bi}_{0.1}\text{Cl}_6$  NCs/TPBi/LiF/Al (Figure 8g). The EL emission spectrum remained unchanged with increasing applied voltage, and the turn-on voltage and maximum luminance of 34.7 cd/m<sup>2</sup> were measured at 10 V. The white  $\text{Cs}_2\text{AgIn}_{0.9}\text{Bi}_{0.1}\text{Cl}_6$  NCs LED exhibited a maximum CE and EQE of 0.058 cd/A and 0.064%, respectively, and emitted white light with CIE chromaticity coordinates (0.32, 0.32) (Figure 8h).

A PeLED utilizing 2D  $\text{Cs}_2\text{AgIn}_x\text{Bi}_{1-x}\text{Cl}_6$  alloyed double perovskite nanoplatelets (NPLs) was also fabricated [189]. A PeLED with the structure ITO/PEDOT: PSS/poly[(9,9-dioctylfluorenyl-2,7-diyl)-co-(4,40-(N-(4-sec-butylphenyl)) diphenylamine)] (TFB)/PVK: NPLs/ZnO/Al was fabricated. To enhance the dispersity of the NPLs and prevent electron leakage into the TFB layer, PVK was employed as a buffer component in the emissive layer, whereas ethanol-based ZnO was spin-coated as the solution-processed ETL. The  $\text{Cs}_2\text{AgIn}_{0.9}\text{Bi}_{0.1}\text{Cl}_6$  NPL-based PeLED exhibited a single EL peak at 557 nm with a maximum luminance of 58 cd/m<sup>2</sup> and an EQE of 0.01%.

#### 4. Conclusions

In this review, we presented a comprehensive overview of recent advances in Pb-free PeNCs and their LED applications. PeNCs exhibit size-tunable properties, high PL efficiency, stability, and large exciton binding energy, making them promising candidates for various optoelectronic applications. However, the toxicity of Pb in LHP NCs has limited their commercialization and driven research on Pb-free MHPs.

We systematically reviewed the crystal structure, synthesis methods, efficient strategies for optoelectronic performance, and LED applications of Pb-free PeNCs based on promising B-site metal candidates as substitutes for Pb. We also discussed the synthetic strategies employed in the development of Pb-free NCs involving the optimization of crystal structures that tune their optoelectronic properties, including the PL characteristics and charge-carrier dynamics mechanism. However, the lower performance and stability, along with a broad emission wavelength of Pb-free PeNCs in comparison to LHP NCs, remain a challenge, and LED applications of Pb-free PeNCs are currently limited. These issues present difficulties for their commercialization.

Therefore, further investigations are required to explore strategies aimed at improving the material stability, optoelectronic properties, and device performance of Pb-free PeNCs. Active research and enhancements need to be undertaken with respect to electrical transport capabilities, optical properties, and stability to contribute to the realization and performance enhancement of LEDs. As mentioned earlier, research endeavors aimed at improving these properties necessitate the further development and utilization of techniques such as doping strategy, ligand exchange, and polymer composites (Figure 9). The directions of this material research could be a promising starting point for improving the performance of Pb-free PeNC-based LEDs. Furthermore, as research progresses on performance, stability improvement, and narrow emission spectra, Pb-free PeNCs will demonstrate the huge potential for LED development, offering prospects for a more sustainable and eco-friendly future in the field of display-related industries.

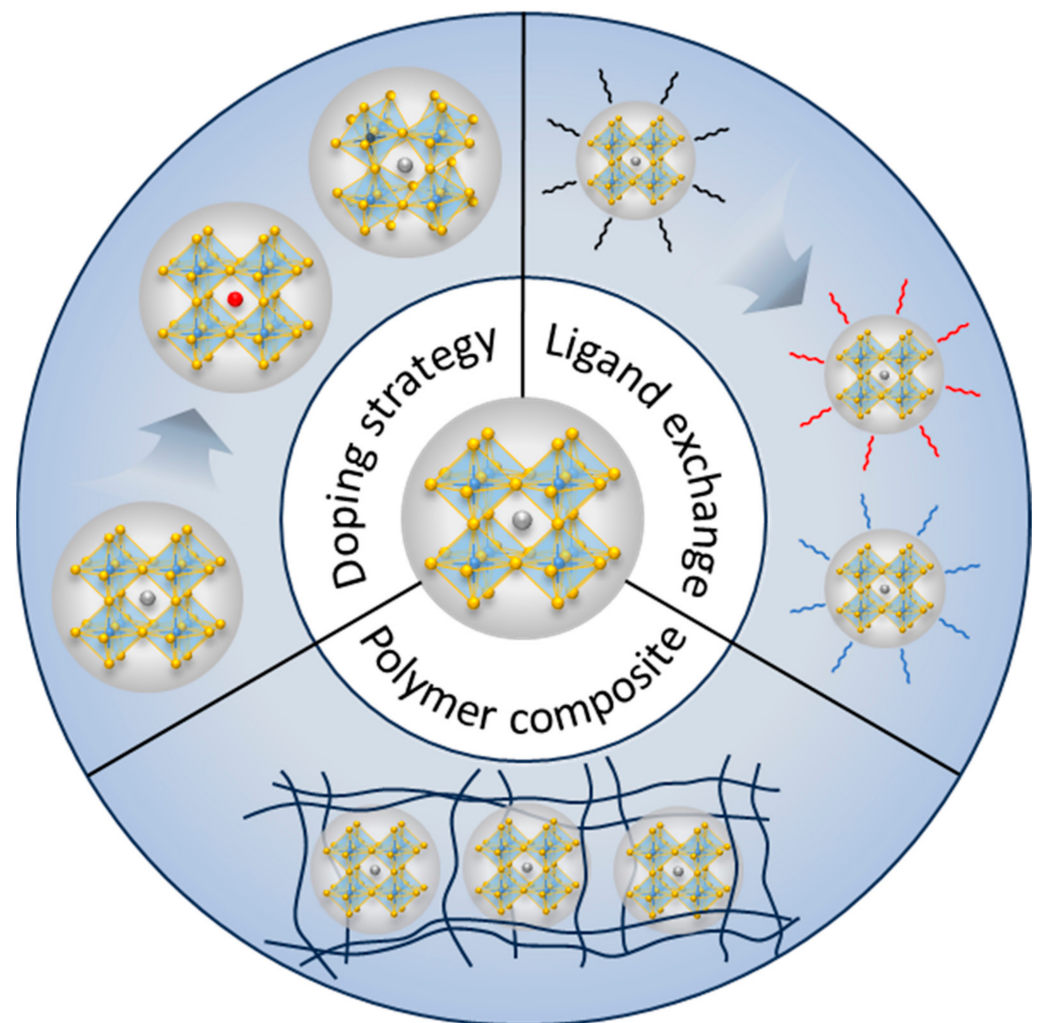


**Figure 9.** Illustration of techniques for enhancing the material properties of PeNCs.

**Author Contributions:** D.-Y.K., J.-G.J., Y.-J.L. and M.-H.P. conceived the outlines and contents; Writing—Original Draft Preparation, D.-Y.K., J.-G.J., and Y.-J.L.; Writing—Review and Editing, D.-Y.K. and M.-H.P.; Supervision, M.-H.P.; Project administration, M.-H.P. All authors have read and agreed to the published version of the manuscript.

**Funding:** This work was mainly supported by Samsung Research Funding, the Incubation Center of Samsung Electronics under Project Number SRFC-TC2103-03, and the Basic Science Research Program through the National Research Foundation of Korea (NRF), funded by the Ministry of Education (2021R1A6A1A10044154).

**Institutional Review Board Statement:** Not applicable.

**Informed Consent Statement:** Not applicable.

**Data Availability Statement:** Not applicable.

**Conflicts of Interest:** The authors declare no conflict of interest.

## References

1. Stranks, S.D.; Snaith, H.J. Metal-Halide Perovskites for Photovoltaic and Light-Emitting Devices. *Nat. Nanotechnol.* **2015**, *10*, 391–402. [[CrossRef](#)] [[PubMed](#)]
2. Xiao, Z.; Kerner, R.A.; Zhao, L.; Tran, N.L.; Lee, K.M.; Koh, T.-W.; Scholes, G.D.; Rand, B.P. Efficient Perovskite Light-Emitting Diodes Featuring Nanometre-Sized Crystallites. *Nat. Photonics* **2017**, *11*, 108–115. [[CrossRef](#)]



3. Liu, X.K.; Xu, W.; Bai, S.; Jin, Y.; Wang, J.; Friend, R.H.; Gao, F. Metal Halide Perovskites for Light-Emitting Diodes. *Nat. Mater.* **2021**, *20*, 10–21. [\[CrossRef\]](#)
4. Park, M.H. 3D and 2D Metal Halide Perovskites for Blue Light-Emitting Diodes. *Materials* **2022**, *15*, 4571. [\[CrossRef\]](#) [\[PubMed\]](#)
5. Lee, M.M.; Teuscher, J.; Miyasaka, T.; Murakami, T.N.; Snaith, H.J. Efficient Hybrid Solar Cells Based on Meso-Superstructured Organometal Halide Perovskites. *Science* **2012**, *338*, 643–647. [\[CrossRef\]](#)
6. Burschka, J.; Pellet, N.; Moon, S.-J.; Humphry-Baker, R.; Gao, P.; Nazeeruddin, M.K.; Grätzel, M. Sequential Deposition as a Route to High-Performance Perovskite-Sensitized Solar Cells. *Nature* **2013**, *499*, 316–319. [\[CrossRef\]](#) [\[PubMed\]](#)
7. Ono, L.K.; Qi, Y.; Liu, S.F. Progress toward Stable Lead Halide Perovskite Solar Cells. *Joule* **2018**, *2*, 1961–1990. [\[CrossRef\]](#)
8. Yakunin, S.; Sytnyk, M.; Kriegner, D.; Shrestha, S.; Richter, M.; Matt, G.J.; Azimi, H.; Brabec, C.J.; Stangl, J.; Kovalenko, M.V.; et al. Detection of X-ray Photons by Solution-Processed Lead Halide Perovskites. *Nat. Photonics* **2015**, *9*, 444–449. [\[CrossRef\]](#)
9. Tian, W.; Zhou, H.; Li, L. Hybrid Organic–Inorganic Perovskite Photodetectors. *Small* **2017**, *13*, 1702107. [\[CrossRef\]](#)
10. Wang, Y.; Li, X.; Nalla, V.; Zeng, H.; Sun, H. Solution-Processed Low Threshold Vertical Cavity Surface Emitting Lasers from All-Inorganic Perovskite Nanocrystals. *Adv. Funct. Mater.* **2017**, *27*, 1605088. [\[CrossRef\]](#)
11. Kanhere, P.; Chen, Z. A Review on Visible Light Active Perovskite-Based Photocatalysts. *Molecules* **2014**, *19*, 19995–20022. [\[CrossRef\]](#) [\[PubMed\]](#)
12. Kim, T.H.; Park, I.; Lee, K.H.; Sim, J.H.; Park, M.H.; Han, T.H.; Paik, U.; Jang, J.; Park, H.B.; Kim, Y.H. Investigating the Interfacial Properties of Halide Perovskite/TiO<sub>x</sub> Heterostructures for Versatile Photocatalytic Reactions under Sunlight. *Nanoscale* **2023**, *15*, 7710–7714. [\[CrossRef\]](#) [\[PubMed\]](#)
13. Liu, H.; Liu, Z.; Xu, W.; Yang, L.; Liu, Y.; Yao, D.; Zhang, D.; Zhang, H.; Yang, B. Engineering the Photoluminescence of CsPbX<sub>3</sub> (X = Cl, Br, and I) Perovskite Nanocrystals Across the Full Visible Spectra with the Interval of 1 Nm. *ACS Appl. Mater. Interfaces* **2019**, *11*, 14256–14265. [\[CrossRef\]](#) [\[PubMed\]](#)
14. Nedelcu, G.; Protesescu, L.; Yakunin, S.; Bodnarchuk, M.I.; Grotevent, M.J.; Kovalenko, M.V. Fast Anion-Exchange in Highly Luminescent Nanocrystals of Cesium Lead Halide Perovskites (CsPbX<sub>3</sub>, X = Cl, Br, I). *Nano Lett.* **2015**, *15*, 5635–5640. [\[CrossRef\]](#) [\[PubMed\]](#)
15. Akkerman, Q.A.; Rainò, G.; Kovalenko, M.V.; Manna, L. Genesis, Challenges and Opportunities for Colloidal Lead Halide Perovskite Nanocrystals. *Nat. Mater.* **2018**, *17*, 394–405. [\[CrossRef\]](#) [\[PubMed\]](#)
16. Huang, H.; Susha, A.S.; Kershaw, S.V.; Hung, T.F.; Rogach, A.L. Control of Emission Color of High Quantum Yield CH<sub>3</sub>NH<sub>3</sub>PbBr<sub>3</sub> Perovskite Quantum Dots by Precipitation Temperature. *Adv. Sci.* **2015**, *2*, 1500194. [\[CrossRef\]](#)
17. Mir, W.J.; Warankar, A.; Acharya, A.; Das, S.; Mandal, P.; Nag, A. Colloidal Thallium Halide Nanocrystals with Reasonable Luminescence, Carrier Mobility and Diffusion Length. *Chem. Sci.* **2017**, *8*, 4602–4611. [\[CrossRef\]](#)
18. Huang, H.; Bodnarchuk, M.I.; Kershaw, S.V.; Kovalenko, M.V.; Rogach, A.L. Lead Halide Perovskite Nanocrystals in the Research Spotlight: Stability and Defect Tolerance. *ACS Energy Lett.* **2017**, *2*, 2071–2083. [\[CrossRef\]](#)
19. Protesescu, L.; Yakunin, S.; Bodnarchuk, M.I.; Krieg, F.; Caputo, R.; Hendon, C.H.; Yang, R.X.; Walsh, A.; Kovalenko, M.V. Nanocrystals of Cesium Lead Halide Perovskites (CsPbX<sub>3</sub>, X = Cl, Br, and I): Novel Optoelectronic Materials Showing Bright Emission with Wide Color Gamut. *Nano Lett.* **2015**, *15*, 3692–3696. [\[CrossRef\]](#)
20. Kovalenko, M.V.; Protesescu, L.; Bodnarchuk, M.I. Properties and Potential Optoelectronic Applications of Lead Halide Perovskite Nanocrystals. *Science* **2017**, *358*, 745–750. [\[CrossRef\]](#)
21. Talapin, D.V.; Lee, J.S.; Kovalenko, M.V.; Shevchenko, E.V. Prospects of Colloidal Nanocrystals for Electronic and Optoelectronic Applications. *Chem. Rev.* **2010**, *110*, 389–458. [\[CrossRef\]](#) [\[PubMed\]](#)
22. Kambhampati, P. Multiexcitons in Semiconductor Nanocrystals: A Platform for Optoelectronics at High Carrier Concentration. *J. Phys. Chem. Lett.* **2012**, *3*, 1182–1190. [\[CrossRef\]](#)
23. Polavarapu, L.; Nickel, B.; Feldmann, J.; Urban, A.S. Advances in Quantum-Confined Perovskite Nanocrystals for Optoelectronics. *Adv. Energy Mater.* **2017**, *7*, 1700267. [\[CrossRef\]](#)
24. Imran, M.; Caligiuri, V.; Wang, M.; Goldoni, L.; Prato, M.; Krahne, R.; De Trizio, L.; Manna, L. Benzoyl Halides as Alternative Precursors for the Colloidal Synthesis of Lead-Based Halide Perovskite Nanocrystals. *J. Am. Chem. Soc.* **2018**, *140*, 2656–2664. [\[CrossRef\]](#) [\[PubMed\]](#)
25. Maddalena, F.; Xie, A.; Chin, X.Y.; Begum, R.; Witkowski, M.E.; Makowski, M.; Mahler, B.; Drozdowski, W.; Springham, S.V.; Rawat, R.S.; et al. Deterministic Light Yield, Fast Scintillation, and Microcolumn Structures in Lead Halide Perovskite Nanocrystals. *J. Phys. Chem. C* **2021**, *125*, 14082–14088. [\[CrossRef\]](#)
26. Wang, Y.; Singh, K.; Li, J.; Dong, Y.; Wang, X.; Pina, J.M.; Yu, Y.; Sabatini, R.; Liu, Y.; Ma, D.; et al. In Situ Inorganic Ligand Replenishment Enables Bandgap Stability in Mixed-Halide Perovskite Quantum Dot Solids. *Adv. Mater.* **2022**, *34*, 2200854. [\[CrossRef\]](#)
27. Kim, J.S.; Heo, J.-M.; Park, G.-S.; Woo, S.-J.; Cho, C.; Yun, H.J.; Kim, D.-H.; Park, J.; Lee, S.-C.; Park, S.-H.; et al. Ultra-Bright, Efficient and Stable Perovskite Light-Emitting Diodes. *Nature* **2022**, *611*, 688–694. [\[CrossRef\]](#)
28. Hao, M.; Bai, Y.; Zeiske, S.; Ren, L.; Liu, J.; Yuan, Y.; Zarrabi, N.; Cheng, N.; Ghasemi, M.; Chen, P.; et al. Ligand-Assisted Cation-Exchange Engineering for High-Efficiency Colloidal Cs<sub>1-x</sub>FA<sub>x</sub>PbI<sub>3</sub> Quantum Dot Solar Cells with Reduced Phase Segregation. *Nat. Energy* **2020**, *5*, 79–88. [\[CrossRef\]](#)
29. Xie, Z.; Park, H.Y.; Kim, H.; Park, J.; Song, D.; Lee, J.; Chetan, L.; Jin, S.H. Stable Dual Cations Perovskite Nanocrystals as Absorbers for Perovskite Solar Cells with Efficiencies Exceeding 24%. *Bull. Korean Chem. Soc.* **2023**, *44*, 658–664. [\[CrossRef\]](#)



30. Kang, C.H.; Dursun, I.; Liu, G.; Sinatra, L.; Sun, X.; Kong, M.; Pan, J.; Maity, P.; Ooi, E.N.; Ng, T.K.; et al. High-Speed Colour-Converting Photodetector with All-Inorganic CsPbBr<sub>3</sub> Perovskite Nanocrystals for Ultraviolet Light Communication. *Light. Sci. Appl.* **2019**, *8*, 94. [\[CrossRef\]](#)
31. Shyamal, S.; Dutta, S.K.; Pradhan, N. Doping Iron in CsPbBr<sub>3</sub> Perovskite Nanocrystals for Efficient and Product Selective CO<sub>2</sub> Reduction. *J. Phys. Chem. Lett.* **2019**, *10*, 7965–7969. [\[CrossRef\]](#) [\[PubMed\]](#)
32. Zhang, X.; Sun, C.; Zhang, Y.; Wu, H.; Ji, C.; Chuai, Y.; Wang, P.; Wen, S.; Zhang, C.; Yu, W.W. Bright Perovskite Nanocrystal Films for Efficient Light-Emitting Devices. *J. Phys. Chem. Lett.* **2016**, *7*, 4602–4610. [\[CrossRef\]](#) [\[PubMed\]](#)
33. Jia, C.; Das, P.; Zeng, Q.; Gabriel, J.C.P.; Tay, C.Y.; Lee, J.M. Activated Recovery of PVC from Contaminated Waste Extension Cord-Cable Using a Weak Acid. *Chemosphere* **2022**, *303*, 134878. [\[CrossRef\]](#)
34. Li, J.; Cao, H.-L.; Jiao, W.-B.; Wang, Q.; Wei, M.; Cantone, I.; Lü, J.; Abate, A. Biological Impact of Lead from Halide Perovskites Reveals the Risk of Introducing a Safe Threshold. *Nat. Commun.* **2020**, *11*, 310. [\[CrossRef\]](#) [\[PubMed\]](#)
35. Wani, A.L.; Ara, A.; Usmani, J.A. Lead Toxicity: A Review. *Interdiscip. Toxicol.* **2015**, *8*, 55–64. [\[CrossRef\]](#) [\[PubMed\]](#)
36. Sun, J.; Yang, J.; Lee, J.I.; Cho, J.H.; Kang, M.S. Lead-Free Perovskite Nanocrystals for Light-Emitting Devices. *J. Phys. Chem. Lett.* **2018**, *9*, 1573–1583. [\[CrossRef\]](#) [\[PubMed\]](#)
37. Zhang, F.; Ma, Z.; Shi, Z.; Chen, X.; Wu, D.; Li, X.; Shan, C. Recent Advances and Opportunities of Lead-Free Perovskite Nanocrystal for Optoelectronic Application. *Energy Mater. Adv.* **2021**, *2021*, 5198145. [\[CrossRef\]](#)
38. Tang, H.; Xu, Y.; Hu, X.; Hu, Q.; Chen, T.; Jiang, W.; Wang, L.; Jiang, W. Lead-Free Halide Double Perovskite Nanocrystals for Light-Emitting Applications: Strategies for Boosting Efficiency and Stability. *Adv. Sci.* **2021**, *8*, 2004118. [\[CrossRef\]](#)
39. Li, X.; Gao, X.; Zhang, X.; Shen, X.; Lu, M.; Wu, J.; Shi, Z.; Colvin, V.L.; Hu, J.; Bai, X.; et al. Lead-Free Halide Perovskites for Light Emission: Recent Advances and Perspectives. *Adv. Sci.* **2021**, *8*, 2003334. [\[CrossRef\]](#)
40. De Souza Carvalho, T.A.; Magalhaes, L.F.; do Livramento Santos, C.I.; de Freitas, T.A.Z.; Carvalho Vale, B.R.; Vale da Fonseca, A.F.; Schiavon, M.A. Lead-Free Metal Halide Perovskite Nanocrystals: From Fundamentals to Applications. *Chem. Eur. J.* **2023**, *29*, e202202518. [\[CrossRef\]](#)
41. Li, C.; Lu, X.; Ding, W.; Feng, L.; Gao, Y.; Guo, Z. Formability of ABX<sub>3</sub> (X = F, Cl, Br, I) Halide Perovskites. *Acta Crystallogr. Sect. B Struct. Sci.* **2008**, *64*, 702–707. [\[CrossRef\]](#) [\[PubMed\]](#)
42. Mao, X.; Sun, L.; Wu, T.; Chu, T.; Deng, W.; Han, K. First-Principles Screening of All-Inorganic Lead-Free ABX<sub>3</sub> Perovskites. *J. Phys. Chem. C* **2018**, *122*, 7670–7675. [\[CrossRef\]](#)
43. Li, C.; Soh, K.C.K.; Wu, P. Formability of ABO<sub>3</sub> Perovskites. *J. Alloys Compd.* **2004**, *372*, 40–48. [\[CrossRef\]](#)
44. Li, W.; Ionescu, E.; Riedel, R.; Gurlo, A. Can We Predict the Formability of Perovskite Oxynitrides from Tolerance and Octahedral Factors? *J. Mater. Chem. A* **2013**, *1*, 12239–12245. [\[CrossRef\]](#)
45. Sun, Q.; Yin, W.J. Thermodynamic Stability Trend of Cubic Perovskites. *J. Am. Chem. Soc.* **2017**, *139*, 14905–14908. [\[CrossRef\]](#)
46. Lin, H.; Zhou, C.; Tian, Y.; Siegrist, T.; Ma, B. Low-Dimensional Organometal Halide Perovskites. *ACS Energy Lett.* **2018**, *3*, 54–62. [\[CrossRef\]](#)
47. Zhou, C.; Lin, H.; He, Q.; Xu, L.; Worku, M.; Chaaban, M.; Lee, S.; Shi, X.; Du, M.H.; Ma, B. Low Dimensional Metal Halide Perovskites and Hybrids. *Mater. Sci. Eng. R Rep.* **2019**, *137*, 38–65. [\[CrossRef\]](#)
48. Luo, S.-Q.; Wang, J.-F.; Yang, B.; Yuan, Y.-B. Recent Advances in Controlling the Crystallization of Two-Dimensional Perovskites for Optoelectronic Device. *Front. Phys.* **2019**, *14*, 53401. [\[CrossRef\]](#)
49. Morss, L.R.; Siegal, M.; Stenger, L.; Edelstein, N. Preparation of Cubic Chloro Complex Compounds of Trivalent Metals: Cs<sub>2</sub>NaMCl<sub>6</sub>. *Inorg. Chem.* **1970**, *9*, 1771–1775. [\[CrossRef\]](#)
50. Kieslich, G.; Sun, S.; Cheetham, A.K. An Extended Tolerance Factor Approach for Organic-Inorganic Perovskites. *Chem. Sci.* **2015**, *6*, 3430–3433. [\[CrossRef\]](#)
51. Filip, M.R.; Giustino, F. Computational Screening of Homovalent Lead Substitution in Organic-Inorganic Halide Perovskites. *J. Phys. Chem. C* **2016**, *120*, 166–173. [\[CrossRef\]](#)
52. Hoefler, S.F.; Trimmel, G.; Rath, T. Progress on Lead-Free Metal Halide Perovskites for Photovoltaic Applications: A Review. *Monatshfte Chem.* **2017**, *148*, 795–826. [\[CrossRef\]](#) [\[PubMed\]](#)
53. Xiao, Z.; Song, Z.; Yan, Y. From Lead Halide Perovskites to Lead-Free Metal Halide Perovskites and Perovskite Derivatives. *Adv. Mater.* **2019**, *31*, e1803792. [\[CrossRef\]](#) [\[PubMed\]](#)
54. Yadav, R.; Srivastava, A.; Abraham, J.A.; Sharma, R.; Dar, S.A. First-Principles Calculations to Investigate Structural, Electronic, Thermoelectric, and Optical Properties of Heavy Thallium Perovskite TIPbX<sub>3</sub> (X = Cl, Br, I). *Mater. Sci. Eng. B Solid-State Mater. Adv. Technol.* **2022**, *283*, 115781. [\[CrossRef\]](#)
55. Ning, W.; Gao, F. Structural and Functional Diversity in Lead-Free Halide Perovskite Materials. *Adv. Mater.* **2019**, *31*, e1900326. [\[CrossRef\]](#) [\[PubMed\]](#)
56. Cheng, Y.-H.; Moriyama, R.; Ebe, H.; Mizuguchi, K.; Yamakado, R.; Nishitsuji, S.; Chiba, T.; Kido, J. Two-Step Crystallization for Low-Oxidation Tin-Based Perovskite Light-Emitting Diodes. *ACS Appl. Mater. Interfaces* **2022**, *14*, 22941–22949. [\[CrossRef\]](#) [\[PubMed\]](#)
57. Chen, M.Y.; Lin, J.T.; Hsu, C.S.; Chang, C.K.; Chiu, C.W.; Chen, H.M.; Chou, P.T. Strongly Coupled Tin-Halide Perovskites to Modulate Light Emission: Tunable 550–640 nm Light Emission (FWHM 36–80 nm) with a Quantum Yield of up to 6.4%. *Adv. Mater.* **2018**, *30*, e1706592. [\[CrossRef\]](#)

58. Liu, Q.; Yin, J.; Zhang, B.B.; Chen, J.K.; Zhou, Y.; Zhang, L.M.; Wang, L.M.; Zhao, Q.; Hou, J.; Shu, J.; et al. Theory-Guided Synthesis of Highly Luminescent Colloidal Cesium Tin Halide Perovskite Nanocrystals. *J. Am. Chem. Soc.* **2021**, *143*, 5470–5480. [\[CrossRef\]](#)
59. Wang, A.; Guo, Y.; Muhammad, F.; Deng, Z. Controlled Synthesis of Lead-Free Cesium Tin Halide Perovskite Cubic Nanocages with High Stability. *Chem. Mater.* **2017**, *29*, 6493–6501. [\[CrossRef\]](#)
60. Giuri, A.; Masi, S.; Listorti, A.; Gigli, G.; Colella, S.; Esposito Corcione, C.; Rizzo, A. Polymeric Rheology Modifier Allows Single-Step Coating of Perovskite Ink for Highly Efficient and Stable Solar Cells. *Nano Energy* **2018**, *54*, 400–408. [\[CrossRef\]](#)
61. Lyu, B.; Guo, X.; Gao, D.; Kou, M.; Yu, Y.; Ma, J.; Chen, S.; Wang, H.; Zhang, Y.; Bao, X. Highly-Stable Tin-Based Perovskite Nanocrystals Produced by Passivation and Coating of Gelatin. *J. Hazard. Mater.* **2021**, *403*, 123967. [\[CrossRef\]](#) [\[PubMed\]](#)
62. Sulaman, M.; Yang, S.Y.; Zhang, Z.H.; Imran, A.; Bukhtiar, A.; Ge, Z.H.; Tang, Y.; Jiang, Y.R.; Tang, L.B.; Zou, B.S. Lead-Free Tin-Based Perovskites Nanocrystals for High-Performance Self-Driven Bulk-Heterojunction Photodetectors. *Mater. Today Phys.* **2022**, *27*, 100829. [\[CrossRef\]](#)
63. Lv, L.; Xu, Y.; Fang, H.; Luo, W.; Xu, F.; Liu, L.; Wang, B.; Zhang, X.; Yang, D.; Hu, W.; et al. Generalized Colloidal Synthesis of High-Quality, Two-Dimensional Cesium Lead Halide Perovskite Nanosheets and Their Applications in Photodetectors. *Nanoscale* **2016**, *8*, 13589–13596. [\[CrossRef\]](#) [\[PubMed\]](#)
64. Zakutayev, A.; Caskey, C.M.; Fioretti, A.N.; Ginley, D.S.; Vidal, J.; Stevanovic, V.; Tea, E.; Lany, S. Defect Tolerant Semiconductors for Solar Energy Conversion. *J. Phys. Chem. Lett.* **2014**, *5*, 1117–1125. [\[CrossRef\]](#) [\[PubMed\]](#)
65. Wu, C.; Zhang, Q.; Liu, G.; Zhang, Z.; Wang, D.; Qu, B.; Chen, Z.; Xiao, L. From Pb to Bi: A Promising Family of Pb-Free Optoelectronic Materials and Devices. *Adv. Energy Mater.* **2020**, *10*, 1902496. [\[CrossRef\]](#)
66. Brandt, R.E.; Stevanović, V.; Ginley, D.S.; Buonassisi, T. Identifying Defect-Tolerant Semiconductors with High Minority-Carrier Lifetimes: Beyond Hybrid Lead Halide Perovskites. *MRS Commun.* **2015**, *5*, 265–275. [\[CrossRef\]](#)
67. Lyu, M.; Yun, J.-H.; Cai, M.; Jiao, Y.; Bernhardt, P.V.; Zhang, M.; Wang, Q.; Du, A.; Wang, H.; Liu, G.; et al. Organic–Inorganic Bismuth (III)-Based Material: A Lead-Free, Air-Stable and Solution-Processable Light-Absorber beyond Organolead Perovskites. *Nano Res.* **2016**, *9*, 692–702. [\[CrossRef\]](#)
68. Hoyer, R.L.Z.; Brandt, R.E.; Osherov, A.; Stevanović, V.; Stranks, S.D.; Wilson, M.W.B.; Kim, H.; Akey, A.J.; Perkins, J.D.; Kurchin, R.C.; et al. Methylammonium Bismuth Iodide as a Lead-Free, Stable Hybrid Organic–Inorganic Solar Absorber. *Chem. Eur. J.* **2016**, *22*, 2605–2610. [\[CrossRef\]](#)
69. Zhang, Y.; Yin, J.; Parida, M.R.; Ahmed, G.H.; Pan, J.; Bakr, O.M.; Brédas, J.-L.; Mohammed, O.F. Direct-Indirect Nature of the Bandgap in Lead-Free Perovskite Nanocrystals. *J. Phys. Chem. Lett.* **2017**, *8*, 3173–3177. [\[CrossRef\]](#)
70. Yang, B.; Chen, J.; Hong, F.; Mao, X.; Zheng, K.; Yang, S.; Li, Y.; Pullerits, T.; Deng, W.; Han, K. Lead-Free, Air-Stable All-Inorganic Cesium Bismuth Halide Perovskite Nanocrystals. *Angew. Chem. Int. Ed.* **2017**, *56*, 12471–12475. [\[CrossRef\]](#)
71. Leng, M.; Chen, Z.; Yang, Y.; Li, Z.; Zeng, K.; Li, K.; Niu, G.; He, Y.; Zhou, Q.; Tang, J. Lead-Free, Blue Emitting Bismuth Halide Perovskite Quantum Dots. *Angew. Chem. Int. Ed.* **2016**, *55*, 15012–15016. [\[CrossRef\]](#) [\[PubMed\]](#)
72. Pal, J.; Bhunia, A.; Chakraborty, S.; Manna, S.; Das, S.; Dewan, A.; Datta, S.; Nag, A. Synthesis and Optical Properties of Colloidal  $M_3Bi_2I_9$  ( $M = Cs, Rb$ ) Perovskite Nanocrystals. *J. Phys. Chem. C* **2018**, *122*, 10643–10649. [\[CrossRef\]](#)
73. Lou, Y.; Fang, M.; Chen, J.; Zhao, Y. Formation of Highly Luminescent Cesium Bismuth Halide Perovskite Quantum Dots Tuned by Anion Exchange. *Chem. Commun.* **2018**, *54*, 3779–3782. [\[CrossRef\]](#) [\[PubMed\]](#)
74. Leng, M.; Yang, Y.; Zeng, K.; Chen, Z.; Tan, Z.; Li, S.; Li, J.; Xu, B.; Li, D.; Hautzinger, M.P.; et al. All-Inorganic Bismuth-Based Perovskite Quantum Dots with Bright Blue Photoluminescence and Excellent Stability. *Adv. Funct. Mater.* **2018**, *28*, 1704446. [\[CrossRef\]](#)
75. Creutz, S.E.; Liu, H.; Kaiser, M.E.; Li, X.; Gamelin, D.R. Structural Diversity in Cesium Bismuth Halide Nanocrystals. *Chem. Mater.* **2019**, *31*, 4685–4697. [\[CrossRef\]](#)
76. Hong, K.-H.; Kim, J.; Debbichi, L.; Kim, H.; Im, S.H. Band Gap Engineering of  $Cs_3Bi_2I_9$  Perovskites with Trivalent Atoms Using a Dual Metal Cation. *J. Phys. Chem. C* **2017**, *121*, 969–974. [\[CrossRef\]](#)
77. Kim, J.; Lee, S.C.; Lee, S.H.; Hong, K.H. Importance of Orbital Interactions in Determining Electronic Band Structures of Organo-Lead Iodide. *J. Phys. Chem. C* **2015**, *119*, 4627–4634. [\[CrossRef\]](#)
78. Lehner, A.J.; Fabini, D.H.; Evans, H.A.; Hébert, C.A.; Smock, S.R.; Hu, J.; Wang, H.; Zwanziger, J.W.; Chabynyc, M.L.; Seshadri, R. Crystal and Electronic Structures of Complex Bismuth Iodides  $A_3Bi_2I_9$  ( $A = K, Rb, Cs$ ) Related to Perovskite: Aiding the Rational Design of Photovoltaics. *Chem. Mater.* **2015**, *27*, 7137–7148. [\[CrossRef\]](#)
79. McCall, K.M.; Stoumpos, C.C.; Kontsevoi, O.Y.; Alexander, G.C.B.; Wessels, B.W.; Kanatzidis, M.G. From 0D  $Cs_3Bi_2I_9$  to 2D  $Cs_3Bi_2I_6Cl_3$ : Dimensional Expansion Induces a Direct Band Gap but Enhances Electron-Phonon Coupling. *Chem. Mater.* **2019**, *31*, 2644–2650. [\[CrossRef\]](#)
80. Yu, B.B.; Liao, M.; Yang, J.; Chen, W.; Zhu, Y.; Zhang, X.; Duan, T.; Yao, W.; Wei, S.H.; He, Z. Alloy-Induced Phase Transition and Enhanced Photovoltaic Performance: The Case of  $Cs_3Bi_2I_{9-x}Br_x$  Perovskite Solar Cells. *J. Mater. Chem. A* **2019**, *7*, 8818–8825. [\[CrossRef\]](#)
81. Hodgkins, T.L.; Savory, C.N.; Bass, K.K.; Seckman, B.L.; Scanlon, D.O.; Djurovich, P.I.; Thompson, M.E.; Melot, B.C. Anionic Order and Band Gap Engineering in Vacancy Ordered Triple Perovskites. *Chem. Commun.* **2019**, *55*, 3164–3167. [\[CrossRef\]](#) [\[PubMed\]](#)
82. Murray, C.B.; Sun, S.; Gaschler, W.; Doyle, H.; Betley, T.A.; Kagan, C.R. Colloidal Synthesis of Nanocrystals and Nanocrystal Superlattices. *IBM J. Res. Dev.* **2001**, *45*, 47–56. [\[CrossRef\]](#)

83. Park, J.; An, K.; Hwang, Y.; Park, J.E.G.; Noh, H.J.; Kim, J.Y.; Park, J.H.; Hwang, N.M.; Hyeon, T. Ultra-Large-Scale Syntheses of Monodisperse Nanocrystals. *Nat. Mater.* **2004**, *3*, 891–895. [[CrossRef](#)] [[PubMed](#)]
84. Jun, Y.W.; Choi, J.S.; Cheon, J. Shape Control of Semiconductor and Metal Oxide Nanocrystals through Nonhydrolytic Colloidal Routes. *Angew. Chem. Int. Ed.* **2006**, *45*, 3414–3439. [[CrossRef](#)]
85. Wang, F.; Han, Y.; Lim, C.S.; Lu, Y.; Wang, J.; Xu, J.; Chen, H.; Zhang, C.; Hong, M.; Liu, X. Simultaneous Phase and Size Control of Upconversion Nanocrystals through Lanthanide Doping. *Nature* **2010**, *463*, 1061–1065. [[CrossRef](#)] [[PubMed](#)]
86. Wu, L.; Chen, S.Y.; Fan, F.J.; Zhuang, T.T.; Dai, C.M.; Yu, S.H. Polytypic Nanocrystals of Cu-Based Ternary Chalcogenides: Colloidal Synthesis and Photoelectrochemical Properties. *J. Am. Chem. Soc.* **2016**, *138*, 5576–5584. [[CrossRef](#)] [[PubMed](#)]
87. Lee, D.; Kim, M.H.; Woo, H.Y.; Chae, J.; Lee, D.; Jeon, S.; Oh, S.J.; Paik, T. Heating-up Synthesis of Cesium Bismuth Bromide Perovskite Nanocrystals with Tailored Composition, Morphology, and Optical Properties. *RSC Adv.* **2020**, *10*, 7126–7133. [[CrossRef](#)] [[PubMed](#)]
88. Liu, M.; Ali-Löytty, H.; Hiltunen, A.; Sarlin, E.; Qudsia, S.; Smått, J.H.; Valden, M.; Vivo, P. Manganese Doping Promotes the Synthesis of Bismuth-Based Perovskite Nanocrystals While Tuning Their Band Structures. *Small* **2021**, *17*, e2100101. [[CrossRef](#)]
89. Meinardi, F.; Akkerman, Q.A.; Bruni, F.; Park, S.; Mauri, M.; Dang, Z.; Manna, L.; Brovelli, S. Doped Halide Perovskite Nanocrystals for Reabsorption-Free Luminescent Solar Concentrators. *ACS Energy Lett.* **2017**, *2*, 2368–2377. [[CrossRef](#)]
90. Qiao, T.; Parobek, D.; Dong, Y.; Ha, E.; Son, D.H. Photoinduced Mn Doping in Cesium Lead Halide Perovskite Nanocrystals. *Nanoscale* **2019**, *11*, 5247–5253. [[CrossRef](#)]
91. Zou, S.; Liu, Y.; Li, J.; Liu, C.; Feng, R.; Jiang, F.; Li, Y.; Song, J.; Zeng, H.; Hong, M.; et al. Stabilizing Cesium Lead Halide Perovskite Lattice through Mn(II) Substitution for Air-Stable Light-Emitting Diodes. *J. Am. Chem. Soc.* **2017**, *139*, 11443–11450. [[CrossRef](#)] [[PubMed](#)]
92. Ali, R.F.; Andreu, I.; Gates, B.D. Green Solvent Assisted Synthesis of Cesium Bismuth Halide Perovskite Nanocrystals and the Influences of Slow and Fast Anion Exchange Rates. *Nanoscale Adv.* **2019**, *1*, 4442–4449. [[CrossRef](#)]
93. McCall, K.M.; Stoumpos, C.C.; Kostina, S.S.; Kanatzidis, M.G.; Wessels, B.W. Strong Electron–Phonon Coupling and Self-Trapped Excitons in the Defect Halide Perovskites  $A_3M_2I_9$  ( $A = Cs, Rb$ ;  $M = Bi, Sb$ ). *Chem. Mater.* **2017**, *29*, 4129–4145. [[CrossRef](#)]
94. Koscher, B.A.; Swabeck, J.K.; Bronstein, N.D.; Alivisatos, A.P. Essentially Trap-Free  $CsPbBr_3$  Colloidal Nanocrystals by Postsynthetic Thiocyanate Surface Treatment. *J. Am. Chem. Soc.* **2017**, *139*, 6566–6569. [[CrossRef](#)] [[PubMed](#)]
95. Leng, M.; Yang, Y.; Chen, Z.; Gao, W.; Zhang, J.; Niu, G.; Li, D.; Song, H.; Zhang, J.; Jin, S.; et al. Surface Passivation of Bismuth-Based Perovskite Variant Quantum Dots To Achieve Efficient Blue Emission. *Nano Lett.* **2018**, *18*, 6076–6083. [[CrossRef](#)] [[PubMed](#)]
96. Wu, Y.; Xiang, G.; Zhang, M.; Wei, D.; Cheng, C.; Leng, J.; Ma, H. Electronic Structures and Photoelectric Properties in  $Cs_3Sb_2X_9$  ( $X = Cl, Br, \text{ or } I$ ) under High Pressure: A First Principles Study. *Nanomaterials* **2022**, *12*, 2982. [[CrossRef](#)] [[PubMed](#)]
97. Zhang, F.; Zhong, H.; Chen, C.; Wu, X.G.; Hu, X.; Huang, H.; Han, J.; Zou, B.; Dong, Y. Brightly Luminescent and Color-Tunable Colloidal  $CH_3NH_3PbX_3$  ( $X = Br, I, Cl$ ) Quantum Dots: Potential Alternatives for Display Technology. *ACS Nano* **2015**, *9*, 4533–4542. [[CrossRef](#)] [[PubMed](#)]
98. Zhang, J.; Yang, Y.; Deng, H.; Farooq, U.; Yang, X.; Khan, J.; Tang, J.; Song, H. High Quantum Yield Blue Emission from Lead-Free Inorganic Antimony Halide Perovskite Colloidal Quantum Dots. *ACS Nano* **2017**, *11*, 9294–9302. [[CrossRef](#)]
99. Shao, H.; Wu, X.; Zhu, J.; Xu, W.; Xu, L.; Dong, B.; Hu, J.; Dong, B.; Bai, X.; Cui, H.; et al.  $Mn^{2+}$  Ions Doped Lead-Free Zero-Dimensional  $K_3SbCl_6$  Perovskite Nanocrystals towards White Light Emitting Diodes. *Chem. Eng. J.* **2021**, *413*, 127415. [[CrossRef](#)]
100. Yang, H.; Santra, S.; Holloway, P.H. Syntheses and Applications of Mn-Doped II–VI Semiconductor Nanocrystals. *J. Nanosci. Nanotechnol.* **2005**, *5*, 1364–1375. [[CrossRef](#)] [[PubMed](#)]
101. Beaulac, R.; Archer, P.I.; Gamelin, D.R. Luminescence in Colloidal  $Mn^{2+}$ -Doped Semiconductor Nanocrystals. *J. Solid. State Chem.* **2008**, *181*, 1582–1589. [[CrossRef](#)]
102. Gao, F.; Zhu, X.; Feng, Q.; Zhong, W.; Liu, W.; Xu, H.; Liu, Y. Deep-Blue Emissive  $Cs_3Cu_2I_5$  Perovskites Nanocrystals with 96.6% Quantum Yield via  $IN_3$ -Assisted Synthesis for Light-Emitting Device and Fluorescent Ink Applications. *Nano Energy* **2022**, *98*, 107270. [[CrossRef](#)]
103. Qu, J.; Xu, S.; Shao, H.; Xia, P.; Lu, C.; Wang, C.; Ban, D. Recent Progress of Copper Halide Perovskites: Properties, Synthesis and Applications. *J. Mater. Chem. C* **2023**, *11*, 6260–6275. [[CrossRef](#)]
104. Wang, M.; Wang, W.; Ma, B.; Shen, W.; Liu, L.; Cao, K.; Chen, S.; Huang, W. Lead-Free Perovskite Materials for Solar Cells. *Nano-Micro Lett.* **2021**, *13*, 62. [[CrossRef](#)] [[PubMed](#)]
105. Hui, Y.; Chen, S.; Lin, R.; Zheng, W.; Huang, F. Photophysics in  $Cs_3Cu_2I_5$  and  $CsCu_2I_3$ . *Mater. Chem. Front.* **2021**, *5*, 7088–7107. [[CrossRef](#)]
106. Yang, P.; Liu, G.; Liu, B.; Liu, X.; Lou, Y.; Chen, J.; Zhao, Y. All-Inorganic  $Cs_2CuX_4$  ( $X = Cl, Br, \text{ and } Br/I$ ) Perovskite Quantum Dots with Blue-Green Luminescence. *Chem. Commun.* **2018**, *54*, 11638–11641. [[CrossRef](#)] [[PubMed](#)]
107. Vashishtha, P.; Nutan, G.V.; Griffith, B.E.; Fang, Y.; Giovanni, D.; Jagadeeswararao, M.; Sum, T.C.; Mathews, N.; Mhaisalkar, S.G.; Hanna, J.V.; et al. Cesium Copper Iodide Tailored Nanoplates and Nanorods for Blue, Yellow, and White Emission. *Chem. Mater.* **2019**, *31*, 9003–9011. [[CrossRef](#)]



108. Cui, W.; Zhao, J.; Wang, L.; Lv, P.; Li, X.; Yin, Z.; Yang, C.; Tang, A. Unraveling the Phase Transition and Luminescence Tuning of Pb-Free Cs-Cu-I Perovskites Enabled by Reaction Temperature and Polar Solvent. *J. Phys. Chem. Lett.* **2022**, *13*, 4856–4863. [[CrossRef](#)] [[PubMed](#)]
109. Hull, S.; Berastegui, P. Crystal Structures and Ionic Conductivities of Ternary Derivatives of the Silver and Copper Monohalides—II: Ordered Phases within the  $(\text{AgX})_x-(\text{MX})_{1-x}$  and  $(\text{CuX})_x-(\text{MX})_{1-x}$  ( $\text{M}=\text{K}, \text{Rb}$  and  $\text{Cs}$ ;  $\text{X}=\text{Cl}, \text{Br}$  and  $\text{I}$ ) Systems. *J. Solid. State Chem.* **2004**, *177*, 3156–3173. [[CrossRef](#)]
110. Vashishtha, P.; Hooper, T.J.N.; Fang, Y.; Kathleen, D.; Giovanni, D.; Klein, M.; Sum, T.C.; Mhaisalkar, S.G.; Mathews, N.; White, T. Room Temperature Synthesis of Low-Dimensional Rubidium Copper Halide Colloidal Nanocrystals with near Unity Photoluminescence Quantum Yield. *Nanoscale* **2021**, *13*, 59–65. [[CrossRef](#)]
111. Lian, L.; Zheng, M.; Zhang, P.; Zheng, Z.; Du, K.; Lei, W.; Gao, J.; Niu, G.; Zhang, D.; Zhai, T.; et al. Photophysics in  $\text{Cs}_3\text{Cu}_2\text{X}_5$  ( $\text{X} = \text{Cl}, \text{Br}, \text{or I}$ ): Highly Luminescent Self-Trapped Excitons from Local Structure Symmetrization. *Chem. Mater.* **2020**, *32*, 3462–3468. [[CrossRef](#)]
112. Xiao, Z.; Du, K.; Meng, W.; Mitzi, D.B.; Yan, Y. Chemical Origin of the Stability Difference between Copper(I)- and Silver(I)-Based Halide Double Perovskites. *Angew. Chem.* **2017**, *129*, 12275–12279. [[CrossRef](#)]
113. Jun, T.; Sim, K.; Iimura, S.; Sasase, M.; Kamioka, H.; Kim, J.; Hosono, H. Lead-Free Highly Efficient Blue-Emitting  $\text{Cs}_3\text{Cu}_2\text{I}_5$  with 0D Electronic Structure. *Adv. Mater.* **2018**, *30*, e1804547. [[CrossRef](#)]
114. Ma, Z.; Shi, Z.; Qin, C.C.; Cui, M.; Yang, D.; Wang, X.; Wang, L.; Ji, X.; Chen, X.; Sun, J.; et al. Stable Yellow Light-Emitting Devices Based on Ternary Copper Halides with Broadband Emissive Self-Trapped Excitons. *ACS Nano* **2020**, *14*, 4475–4486. [[CrossRef](#)] [[PubMed](#)]
115. Du, M.H. Emission Trend of Multiple Self-Trapped Excitons in Luminescent 1D Copper Halides. *ACS Energy Lett.* **2020**, *5*, 464–469. [[CrossRef](#)]
116. Li, S.; Luo, J.; Liu, J.; Tang, J. Self-Trapped Excitons in All-Inorganic Halide Perovskites: Fundamentals, Status, and Potential Applications. *J. Phys. Chem. Lett.* **2019**, *10*, 1999–2007. [[CrossRef](#)] [[PubMed](#)]
117. Zhang, X.; Zhou, B.; Chen, X.; Yu, W.W. Reversible Transformation between  $\text{Cs}_3\text{Cu}_2\text{I}_5$  and  $\text{CsCu}_2\text{I}_3$  Perovskite Derivatives and Its Anticounterfeiting Application. *Inorg. Chem.* **2022**, *61*, 399–405. [[CrossRef](#)]
118. Cheng, P.; Sun, L.; Feng, L.; Yang, S.; Yang, Y.; Zheng, D.; Zhao, Y.; Sang, Y.; Zhang, R.; Wei, D.; et al. Colloidal Synthesis and Optical Properties of All-Inorganic Low-Dimensional Cesium Copper Halide Nanocrystals. *Angew. Chem.* **2019**, *131*, 16233–16237. [[CrossRef](#)]
119. Liu, S.; Liu, H.; Zhou, G.; Li, X.; Wang, S. Water-Induced Crystal Phase Transformation of Stable Lead-Free Cu-Based Perovskite Nanocrystals Prepared by One-Pot Method. *Chem. Eng. J.* **2022**, *427*, 131430. [[CrossRef](#)]
120. Creason, T.D.; McWhorter, T.M.; Bell, Z.; Du, M.H.; Saparov, B.  $\text{K}_2\text{CuX}_3$  ( $\text{X} = \text{Cl}, \text{Br}$ ): All-Inorganic Lead-Free Blue Emitters with Near-Unity Photoluminescence Quantum Yield. *Chem. Mater.* **2020**, *32*, 6197–6205. [[CrossRef](#)]
121. Li, Y.; Vashishtha, P.; Zhou, Z.; Li, Z.; Shivarudraiah, S.B.; Ma, C.; Liu, J.; Wong, K.S.; Su, H.; Halpert, J.E. Room Temperature Synthesis of Stable, Printable  $\text{Cs}_3\text{Cu}_2\text{X}_5$  ( $\text{X} = \text{I}, \text{Br/I}, \text{Br}, \text{Br/Cl}, \text{Cl}$ ) Colloidal Nanocrystals with Near-Unity Quantum Yield Green Emitters ( $\text{X} = \text{Cl}$ ). *Chem. Mater.* **2020**, *32*, 5515–5524. [[CrossRef](#)]
122. Zhao, Z.; Li, X.; Xie, L.; Chen, B.; Jiang, T.; Cao, J.; Zhang, F.; Wang, M.; Wu, Y.; Zheng, H.; et al. Phase Control in the Synthesis of Cesium Copper Iodide Compounds for Their Photoluminescence and Radioluminescence Study. *J. Lumin.* **2022**, *241*, 118482. [[CrossRef](#)]
123. Qu, K.; Lu, Y.; Ran, P.; Wang, K.; Zhang, N.; Xia, K.; Zhang, H.; Pi, X.; Hu, H.; Yang, Y.; et al. Zn (II)-Doped Cesium Copper Halide Nanocrystals with High Quantum Yield and Colloidal Stability for High-Resolution X-Ray Imaging. *Adv. Opt. Mater.* **2023**, *11*, 2202883. [[CrossRef](#)]
124. Cai, T.; Shi, W.; Hwang, S.; Kobbekaduwa, K.; Nagaoka, Y.; Yang, H.; Hills-Kimball, K.; Zhu, H.; Wang, J.; Wang, Z.; et al. Lead-Free  $\text{Cs}_4\text{CuSb}_2\text{Cl}_{12}$  Layered Double Perovskite Nanocrystals. *J. Am. Chem. Soc.* **2020**, *142*, 11927–11936. [[CrossRef](#)] [[PubMed](#)]
125. Slavney, A.H.; Hu, T.; Lindenberg, A.M.; Karunadasa, H.I. A Bismuth-Halide Double Perovskite with Long Carrier Recombination Lifetime for Photovoltaic Applications. *J. Am. Chem. Soc.* **2016**, *138*, 2138–2141. [[CrossRef](#)] [[PubMed](#)]
126. McClure, E.T.; Ball, M.R.; Windl, W.; Woodward, P.M.  $\text{Cs}_2\text{AgBiX}_6$  ( $\text{X} = \text{Br}, \text{Cl}$ ): New Visible Light Absorbing, Lead-Free Halide Perovskite Semiconductors. *Chem. Mater.* **2016**, *28*, 1348–1354. [[CrossRef](#)]
127. Zhou, J.; Xia, Z.; Molokeev, M.S.; Zhang, X.; Peng, D.; Liu, Q. Composition Design, Optical Gap and Stability Investigations of Lead-Free Halide Double Perovskite  $\text{Cs}_2\text{AgInCl}_6$ . *J. Mater. Chem. A* **2017**, *5*, 15031–15037. [[CrossRef](#)]
128. Zhou, L.; Xu, Y.F.; Chen, B.X.; Kuang, D.B.; Su, C.Y. Synthesis and Photocatalytic Application of Stable Lead-Free  $\text{Cs}_2\text{AgBiBr}_6$  Perovskite Nanocrystals. *Small* **2018**, *14*, e1703762. [[CrossRef](#)]
129. Xiao, Z.; Meng, W.; Wang, J.; Yan, Y. Thermodynamic Stability and Defect Chemistry of Bismuth-Based Lead-Free Double Perovskites. *ChemSusChem* **2016**, *9*, 2628–2633. [[CrossRef](#)]
130. Meng, W.; Wang, X.; Xiao, Z.; Wang, J.; Mitzi, D.B.; Yan, Y. Parity-Forbidden Transitions and Their Impact on the Optical Absorption Properties of Lead-Free Metal Halide Perovskites and Double Perovskites. *J. Phys. Chem. Lett.* **2017**, *8*, 2999–3007. [[CrossRef](#)]
131. Volonakis, G.; Haghighirad, A.A.; Milot, R.L.; Sio, W.H.; Filip, M.R.; Wenger, B.; Johnston, M.B.; Herz, L.M.; Snaith, H.J.; Giustino, F.  $\text{Cs}_2\text{InAgCl}_6$ : A New Lead-Free Halide Double Perovskite with Direct Band Gap. *J. Phys. Chem. Lett.* **2017**, *8*, 772–778. [[CrossRef](#)]



132. Yang, B.; Chen, J.; Yang, S.; Hong, F.; Sun, L.; Han, P.; Pullerits, T.; Deng, W.; Han, K. Lead-Free Silver-Bismuth Halide Double Perovskite Nanocrystals. *Angew. Chem. Int. Ed.* **2018**, *57*, 5359–5363. [[CrossRef](#)] [[PubMed](#)]
133. Creutz, S.E.; Crites, E.N.; De Siena, M.C.; Gamelin, D.R. Colloidal Nanocrystals of Lead-Free Double-Perovskite (Elpasolite) Semiconductors: Synthesis and Anion Exchange to Access New Materials. *Nano Lett.* **2018**, *18*, 1118–1123. [[CrossRef](#)]
134. Yang, B.; Mao, X.; Hong, F.; Meng, W.; Tang, Y.; Xia, X.; Yang, S.; Deng, W.; Han, K. Lead-Free Direct Band Gap Double-Perovskite Nanocrystals with Bright Dual-Color Emission. *J. Am. Chem. Soc.* **2018**, *140*, 17001–17006. [[CrossRef](#)] [[PubMed](#)]
135. Bekenstein, Y.; Dahl, J.C.; Huang, J.; Osowiecki, W.T.; Swabeck, J.K.; Chan, E.M.; Yang, P.; Alivisatos, A.P. The Making and Breaking of Lead-Free Double Perovskite Nanocrystals of Cesium Silver-Bismuth Halide Compositions. *Nano Lett.* **2018**, *18*, 3502–3508. [[CrossRef](#)] [[PubMed](#)]
136. Hutter, E.M.; Gélvez-Rueda, M.C.; Oshero, A.; Bulović, V.; Grozema, F.C.; Stranks, S.D.; Savenije, T.J. Direct-Indirect Character of the Bandgap in Methylammonium Lead Iodide Perovskite. *Nat. Mater.* **2017**, *16*, 115–120. [[CrossRef](#)] [[PubMed](#)]
137. Manna, D.; Das, T.K.; Yella, A. Tunable and Stable White Light Emission in Bi<sup>3+</sup>-Alloyed Cs<sub>2</sub>AgInCl<sub>6</sub> Double Perovskite Nanocrystals. *Chem. Mater.* **2019**, *31*, 10063–10070. [[CrossRef](#)]
138. Guo, F.; Lu, Z.; Mohanty, D.; Wang, T.; Bhat, I.B.; Zhang, S.; Shi, S.; Washington, M.A.; Wang, G.C.; Lu, T.M. A Two-Step Dry Process for Cs<sub>2</sub>SnI<sub>6</sub> Perovskite Thin Film. *Mater. Res. Lett.* **2017**, *5*, 540–546. [[CrossRef](#)]
139. Ke, J.C.R.; Lewis, D.J.; Walton, A.S.; Spencer, B.F.; O'Brien, P.; Thomas, A.G.; Flavell, W.R. Ambient-Air-Stable Inorganic Cs<sub>2</sub>SnI<sub>6</sub> Double Perovskite Thin Films: Via Aerosol-Assisted Chemical Vapour Deposition. *J. Mater. Chem. A* **2018**, *6*, 11205–11214. [[CrossRef](#)]
140. Shin, H.O.; Kim, B.M.; Jang, T.; Kim, K.M.; Roh, D.H.; Nam, J.S.; Kim, J.S.; Kim, U.Y.; Lee, B.; Pang, Y.; et al. Surface State-Mediated Charge Transfer of Cs<sub>2</sub>SnI<sub>6</sub> and Its Application in Dye-Sensitized Solar Cells. *Adv. Energy Mater.* **2019**, *9*, 1803243. [[CrossRef](#)]
141. Wang, A.; Yan, X.; Zhang, M.; Sun, S.; Yang, M.; Shen, W.; Pan, X.; Wang, P.; Deng, Z. Controlled Synthesis of Lead-Free and Stable Perovskite Derivative Cs<sub>2</sub>SnI<sub>6</sub> Nanocrystals via a Facile Hot-Injection Process. *Chem. Mater.* **2016**, *28*, 8132–8140. [[CrossRef](#)]
142. Pan, A.; He, B.; Fan, X.; Liu, Z.; Urban, J.J.; Alivisatos, A.P.; He, L.; Liu, Y. Insight into the Ligand-Mediated Synthesis of Colloidal CsPbBr<sub>3</sub> Perovskite Nanocrystals: The Role of Organic Acid, Base, and Cesium Precursors. *ACS Nano* **2016**, *10*, 7943–7954. [[CrossRef](#)] [[PubMed](#)]
143. Haydous, F.; Gardner, J.M.; Cappel, U.B. The Impact of Ligands on the Synthesis and Application of Metal Halide Perovskite Nanocrystals. *J. Mater. Chem. A* **2021**, *9*, 23419–23443. [[CrossRef](#)]
144. Xu, Y.; Li, S.; Zhang, Z.; Hu, Y.; Yuan, L.; Chen, W.; Chen, Z.; Patterson, R.; Huang, S. Ligand-Mediated Synthesis of Colloidal Cs<sub>2</sub>SnI<sub>6</sub> Three-Dimensional Nanocrystals and Two-Dimensional Nanoplatelets. *Nanotechnology* **2019**, *30*, 295601. [[CrossRef](#)] [[PubMed](#)]
145. Muljarov, E.A.; Tikhodeev, S.G.; Gippius, N.A.; Ishihara, T. Excitons in Self-Organized Semiconductor/Insulator Superlattices: PbI<sub>2</sub>-Based Perovskite Compounds. *Phys. Rev. B* **1995**, *51*, 14370–14378. [[CrossRef](#)] [[PubMed](#)]
146. Goto, T.; Makino, H.; Yao, T.; Chia, C.H.; Makino, T.; Segawa, Y.; Mousdis, G.A.; Papavassiliou, G.C. Localization of Triplet Excitons and Biexcitons in the Two-Dimensional Semiconductor (CH<sub>3</sub>C<sub>6</sub>H<sub>4</sub>CH<sub>2</sub>NH<sub>3</sub>)<sub>2</sub>PbBr<sub>4</sub>. *Phys. Rev. B* **2006**, *73*, 115206. [[CrossRef](#)]
147. Jing, Y.; Liu, Y.; Zhao, J.; Xia, Z. Sb<sup>3+</sup> Doping-Induced Triplet Self-Trapped Excitons Emission in Lead-Free Cs<sub>2</sub>SnCl<sub>6</sub> Nanocrystals. *J. Phys. Chem. Lett.* **2019**, *10*, 7439–7444. [[CrossRef](#)]
148. Vargas, B.; Ramos, E.; Pérez-Gutiérrez, E.; Alonso, J.C.; Solís-Ibarra, D. A Direct Bandgap Copper-Antimony Halide Perovskite. *J. Am. Chem. Soc.* **2017**, *139*, 9116–9119. [[CrossRef](#)]
149. Vargas, B.; Torres-Cadena, R.; Rodríguez-Hernández, J.; Gembicky, M.; Xie, H.; Jiménez-Mier, J.; Liu, Y.S.; Menéndez-Proupin, E.; Dunbar, K.R.; Lopez, N.; et al. Optical, Electronic, and Magnetic Engineering of «111» Layered Halide Perovskites. *Chem. Mater.* **2018**, *30*, 5315–5321. [[CrossRef](#)]
150. Singhal, N.; Chakraborty, R.; Ghosh, P.; Nag, A. Low-Bandgap Cs<sub>4</sub>CuSb<sub>2</sub>Cl<sub>12</sub> Layered Double Perovskite: Synthesis, Reversible Thermal Changes, and Magnetic Interaction. *Chem. Asian J.* **2018**, *13*, 2085–2092. [[CrossRef](#)]
151. Vargas, B.; Torres-Cadena, R.; Reyes-Castillo, D.T.; Rodríguez-Hernández, J.; Gembicky, M.; Menéndez-Proupin, E.; Solís-Ibarra, D. Chemical Diversity in Lead-Free, Layered Double Perovskites: A Combined Experimental and Computational Approach. *Chem. Mater.* **2020**, *32*, 424–429. [[CrossRef](#)]
152. Yang, H.; Shi, W.; Cai, T.; Hills-Kimball, K.; Liu, Z.; Dube, L.; Chen, O. Synthesis of Lead-Free Cs<sub>4</sub>(Cd<sub>1-x</sub>Mn<sub>x</sub>)Bi<sub>2</sub>Cl<sub>12</sub> (0 ≤ x ≤ 1) Layered Double Perovskite Nanocrystals with Controlled Mn-Mn Coupling Interaction. *Nanoscale* **2020**, *12*, 23191–23199. [[CrossRef](#)] [[PubMed](#)]
153. Peng, C.; Wei, Q.; Chen, L.; Zeng, R.; Zhang, Q.; Hu, Q.; Zou, B. Efficient Energy Transfer in Cs<sub>4</sub>Mn<sub>x</sub>Cd<sub>1-x</sub>Sb<sub>2</sub>Cl<sub>12</sub> layered Perovskites and Anomalously Responsive Photodetectors. *J. Mater. Chem. C* **2021**, *9*, 15522–15529. [[CrossRef](#)]
154. Cai, T.; Shi, W.; Gosztola, D.J.; Kobbekaduwa, K.; Yang, H.; Jin, N.; Nagaoka, Y.; Dube, L.; Schneider, J.; Hwang, S.; et al. Colloidal Synthesis and Charge Carrier Dynamics of Cs<sub>4</sub>Cd<sub>1-x</sub>Cu<sub>x</sub>Sb<sub>2</sub>Cl<sub>12</sub> (0 ≤ x ≤ 1) Layered Double Perovskite Nanocrystals. *Matter* **2021**, *4*, 2936–2952. [[CrossRef](#)]
155. Sartori, E.; Campolucci, M.; Baranov, D.; Zeng, M.; Toso, S.; Divitini, G.; Ferretti, M.; Hens, Z.; Manna, L.; Locardi, F. Red-Emissive Nanocrystals of Cs<sub>4</sub>Mn<sub>x</sub>Cd<sub>1-x</sub>Sb<sub>2</sub>Cl<sub>12</sub> layered Perovskites. *Nanoscale* **2022**, *14*, 305–311. [[CrossRef](#)]
156. Sawahreh, A.; Binyamin, T.; Jiang, J.; Millo, O.; Goldberg, O.; Azulay, D.; Pachter, R.; Etgar, L. Electrical and Chemical Properties of Vacancy-Ordered Lead Free Layered Double Perovskite Nanoparticles. *Nanoscale* **2022**, *14*, 3487–3495. [[CrossRef](#)] [[PubMed](#)]

157. Bhardwaj, A.; Kundu, K.; Sasmal, R.; Acharyya, P.; Pradhan, J.; Kalita, S.; Agasti, S.S.; Biswas, K. 2D Nanosheets of Layered Double Perovskites: Synthesis, Photostable Bright Orange Emission and Photoluminescence Blinking. *Chem. Sci.* **2023**, *14*, 7161–7169. [[CrossRef](#)] [[PubMed](#)]
158. Richter, J.M.; Abdi-Jalebi, M.; Sadhanala, A.; Tabachnyk, M.; Rivett, J.P.H.; Pazos-Outón, L.M.; Gödel, K.C.; Price, M.; Deschler, F.; Friend, R.H. Enhancing Photoluminescence Yields in Lead Halide Perovskites by Photon Recycling and Light Out-Coupling. *Nat. Commun.* **2016**, *7*, 13941. [[CrossRef](#)]
159. Klimov, V.I.; Mikhailovsky, A.A.; McBranch, D.W.; Leatherdale, C.A.; Bawendi, M.G. Quantization of Multiparticle Auger Rates in Semiconductor Quantum Dots. *Science* **2000**, *287*, 1011–1013. [[CrossRef](#)]
160. Milot, R.L.; Sutton, R.J.; Eperon, G.E.; Haghighirad, A.A.; Martinez Hardigree, J.; Miranda, L.; Snaith, H.J.; Johnston, M.B.; Herz, L.M. Charge-Carrier Dynamics in 2D Hybrid Metal–Halide Perovskites. *Nano Lett.* **2016**, *16*, 7001–7007. [[CrossRef](#)]
161. Zou, W.; Li, R.; Zhang, S.; Liu, Y.; Wang, N.; Cao, Y.; Miao, Y.; Xu, M.; Guo, Q.; Di, D.; et al. Minimising Efficiency Roll-off in High-Brightness Perovskite Light-Emitting Diodes. *Nat. Commun.* **2018**, *9*, 608. [[CrossRef](#)] [[PubMed](#)]
162. Suyver, J.F.; Wuister, S.F.; Kelly, J.J.; Meijerink, A. Luminescence of Nanocrystalline ZnSe:Mn<sup>2+</sup>. *Phys. Chem. Chem. Phys.* **2000**, *2*, 5445–5448. [[CrossRef](#)]
163. Liu, H.; Wu, Z.; Shao, J.; Yao, D.; Gao, H.; Liu, Y.; Yu, W.; Zhang, H.; Yang, B. CsPb<sub>x</sub>Mn<sub>1-x</sub>Cl<sub>3</sub> Perovskite Quantum Dots with High Mn Substitution Ratio. *ACS Nano* **2017**, *11*, 2239–2247. [[CrossRef](#)] [[PubMed](#)]
164. Liu, Y.; Jing, Y.; Zhao, J.; Liu, Q.; Xia, Z. Design Optimization of Lead-Free Perovskite Cs<sub>2</sub>AgInCl<sub>6</sub>:Bi Nanocrystals with 11.4% Photoluminescence Quantum Yield. *Chem. Mater.* **2019**, *31*, 3333–3339. [[CrossRef](#)]
165. Zhang, H.; Zhu, L.; Cheng, J.; Chen, L.; Liu, C.; Yuan, S. Photoluminescence Characteristics of Sn<sup>2+</sup> and Ce<sup>3+</sup>-Doped Cs<sub>2</sub>SnCl<sub>6</sub> Double-Perovskite Crystals. *Materials* **2019**, *12*, 1501. [[CrossRef](#)] [[PubMed](#)]
166. Li, J.; Tan, Z.; Hu, M.; Chen, C.; Luo, J.; Li, S.; Gao, L.; Xiao, Z.; Niu, G.; Tang, J. Antimony Doped Cs<sub>2</sub>SnCl<sub>6</sub> with Bright and Stable Emission. *Front. Optoelectron.* **2019**, *12*, 352–364. [[CrossRef](#)]
167. Zhou, J.; Rong, X.; Zhang, P.; Molokeev, M.S.; Wei, P.; Liu, Q.; Zhang, X.; Xia, Z. Manipulation of Bi<sup>3+</sup>/In<sup>3+</sup> Transmutation and Mn<sup>2+</sup>-Doping Effect on the Structure and Optical Properties of Double Perovskite Cs<sub>2</sub>NaBi<sub>1-x</sub>In<sub>x</sub>Cl<sub>6</sub>. *Adv. Opt. Mater.* **2019**, *7*, 1801435. [[CrossRef](#)]
168. Lin, T.W.; Su, C.; Lin, C.C. Phase Transition and Energy Transfer of Lead-Free Cs<sub>2</sub>SnCl<sub>6</sub> Perovskite Nanocrystals by Controlling the Precursors and Doping Manganese Ions. *J. Inf. Disp.* **2019**, *20*, 209–216. [[CrossRef](#)]
169. Noculak, A.; Noculak, A.; Morad, V.; Morad, V.; McCall, K.M.; Yakunin, S.; Shynkarenko, Y.; Yakunin, S.; Shynkarenko, Y.; Wörle, M.; et al. Bright Blue and Green Luminescence of Sb(III) in Double Perovskite Cs<sub>2</sub>MInCl<sub>6</sub> (M = Na, K) Matrices. *Chem. Mater.* **2020**, *32*, 5118–5124. [[CrossRef](#)]
170. Tan, Z.; Chu, Y.; Chen, J.; Li, J.; Ji, G.; Niu, G.; Gao, L.; Xiao, Z.; Tang, J. Lead-Free Perovskite Variant Solid Solutions Cs<sub>2</sub>Sn<sub>1-x</sub>TeXCl<sub>6</sub>: Bright Luminescence and High Anti-Water Stability. *Adv. Mater.* **2020**, *32*, e2002443. [[CrossRef](#)]
171. Koyanagi, T.; Kapil, G.; Ogomi, Y.; Yoshino, K.; Shen, Q.; Toyoda, T.; Murakami, T.N.; Segawa, H.; Hayase, S. Hot-Injection and Ultrasonic Irradiation Syntheses of Cs<sub>2</sub>SnI<sub>6</sub> Quantum Dot Using Sn Long-Chain Amino-Complex. *J. Nanoparticle Res.* **2020**, *22*, 69. [[CrossRef](#)]
172. Holzapfel, N.P.; Majher, J.D.; Strom, T.A.; Moore, C.E.; Woodward, P.M. Cs<sub>4</sub>Cd<sub>1-x</sub>Mn<sub>x</sub>Bi<sub>2</sub>Cl<sub>12</sub>- A Vacancy-Ordered Halide Perovskite Phosphor with High-Efficiency Orange-Red Emission. *Chem. Mater.* **2020**, *32*, 3510–3516. [[CrossRef](#)]
173. Vargas, B.; Reyes-Castillo, D.T.; Coutino-Gonzalez, E.; Sánchez-Aké, C.; Ramos, C.; Falcony, C.; Solis-Ibarra, D. Enhanced Luminescence and Mechanistic Studies on Layered Double-Perovskite Phosphors: Cs<sub>4</sub>Cd<sub>1-x</sub>Mn<sub>x</sub>Bi<sub>2</sub>Cl<sub>12</sub>. *Chem. Mater.* **2020**, *32*, 9307–9315. [[CrossRef](#)]
174. Zheng, W.; Sun, R.; Liu, Y.; Wang, X.; Liu, N.; Ji, Y.; Wang, L.; Liu, H.; Zhang, Y. Excitation Management of Lead-Free Perovskite Nanocrystals through Doping. *ACS Appl. Mater. Interfaces* **2021**, *13*, 6404–6410. [[CrossRef](#)] [[PubMed](#)]
175. Levy, S.; Khalfin, S.; Pavlopoulos, N.G.; Kauffmann, Y.; Atiya, G.; Shaek, S.; Dror, S.; Shechter, R.; Bekenstein, Y. The Role Silver Nanoparticles Plays in Silver-Based Double-Perovskite Nanocrystals. *Chem. Mater.* **2021**, *33*, 2370–2377. [[CrossRef](#)] [[PubMed](#)]
176. Ahmad, R.; Zdražil, L.; Kalytchuk, S.; Naldoni, A.; Rogach, A.L.; Schmuki, P.; Zboril, R.; Kment, Š. Uncovering the Role of Trioctylphosphine on Colloidal and Emission Stability of Sb-Alloyed Cs<sub>2</sub>NaInCl<sub>6</sub> Double Perovskite Nanocrystals. *ACS Appl. Mater. Interfaces* **2021**, *13*, 47845–47859. [[CrossRef](#)] [[PubMed](#)]
177. Shen, J.; Zhu, W.; Lian, Z.; Lin, A.; Shi, S.F.; Yang, K.; Li, M.; Zhao, D.; Sun, Y.Y.; Lian, J. Metal Ion-Incorporated Lead-Free Perovskites toward Broadband Photodetectors. *ACS Appl. Electron. Mater.* **2023**. [[CrossRef](#)]
178. Liu, M.; Matta, S.K.; Ali-Löytty, H.; Matuhina, A.; Grandhi, G.K.; Lahtonen, K.; Russo, S.P.; Vivo, P. Moisture-Assisted near-UV Emission Enhancement of Lead-Free Cs<sub>4</sub>CuIn<sub>2</sub>Cl<sub>12</sub> Double Perovskite Nanocrystals. *Nano Lett.* **2022**, *22*, 311–318. [[CrossRef](#)]
179. Cui, E.; Yuan, X.; Tang, L.; Yang, L.; Yang, X.; Liao, X.; Tang, J.; Zhao, Y.; Sun, W.; Liu, K.; et al. Eu<sup>3+</sup>, Tb<sup>3+</sup> Doping Induced Tunable Luminescence of Cs<sub>2</sub>AgInCl<sub>6</sub> Double Perovskite Nanocrystals and Its Mechanism. *Appl. Surf. Sci.* **2023**, *609*, 155472. [[CrossRef](#)]
180. Dolzhnikov, D.S.; Wang, C.; Xu, Y.; Kanatzidis, M.G.; Weiss, E.A. Ligand-Free, Quantum-Confined Cs<sub>2</sub>SnI<sub>6</sub> Perovskite Nanocrystals. *Chem. Mater.* **2017**, *29*, 7901–7907. [[CrossRef](#)]
181. Tang, G.; Xiao, Z.; Hosono, H.; Kamiya, T.; Fang, D.; Hong, J. Layered Halide Double Perovskites Cs<sub>3+n</sub>M(II)<sub>n</sub>Sb<sub>2</sub>X<sub>9+3n</sub> (M = Sn, Ge) for Photovoltaic Applications. *J. Phys. Chem. Lett.* **2018**, *9*, 43–48. [[CrossRef](#)] [[PubMed](#)]

182. Tan, Z.; Li, J.; Zhang, C.; Li, Z.; Hu, Q.; Xiao, Z.; Kamiya, T.; Hosono, H.; Niu, G.; Lifshitz, E.; et al. Highly Efficient Blue-Emitting Bi-Doped Cs<sub>2</sub>SnCl<sub>6</sub> Perovskite Variant: Photoluminescence Induced by Impurity Doping. *Adv. Funct. Mater.* **2018**, *28*, 1801131. [[CrossRef](#)]
183. Mu, H.; Hu, F.; Wang, R.; Jia, J.; Xiao, S. Effects of In-Situ Annealing on the Electroluminescence Performance of the Sn-Based Perovskite Light-Emitting Diodes Prepared by Thermal Evaporation. *J. Lumin.* **2020**, *226*, 117493. [[CrossRef](#)]
184. Mahesh, K.P.O.; Chang, C.-Y.; Hong, W.-L.; Wen, T.-H.; Lo, P.-H.; Chiu, H.-Z.; Hsu, C.-L.; Horng, S.-F.; Chao, Y.-C. Lead-Free Cesium Tin Halide Nanocrystals for Light-Emitting Diodes and Color down Conversion. *RSC Adv.* **2020**, *10*, 37161–37167. [[CrossRef](#)] [[PubMed](#)]
185. Zhang, X.; Wang, C.; Zhang, Y.; Zhang, X.; Wang, S.; Lu, M.; Cui, H.; Kershaw, S.V.; Yu, W.W.; Rogach, A.L. Bright Orange Electroluminescence from Lead-Free Two-Dimensional Perovskites. *ACS Energy Lett.* **2019**, *4*, 242–248. [[CrossRef](#)]
186. Ma, Z.; Shi, Z.; Yang, D.; Zhang, F.; Li, S.; Wang, L.; Wu, D.; Zhang, Y.; Na, G.; Zhang, L.; et al. Electrically-Driven Violet Light-Emitting Devices Based on Highly Stable Lead-Free Perovskite Cs<sub>3</sub>Sb<sub>2</sub>Br<sub>9</sub> Quantum Dots. *ACS Energy Lett.* **2020**, *5*, 385–394. [[CrossRef](#)]
187. Wang, L.; Shi, Z.; Ma, Z.; Yang, D.; Zhang, F.; Ji, X.; Wang, M.; Chen, X.; Na, G.; Chen, S.; et al. Colloidal Synthesis of Ternary Copper Halide Nanocrystals for High-Efficiency Deep-Blue Light-Emitting Diodes with a Half-Lifetime above 100 H. *Nano Lett.* **2020**, *20*, 3568–3576. [[CrossRef](#)]
188. Zhang, Y.; Zhang, Z.; Yu, W.; He, Y.; Chen, Z.; Xiao, L.; Shi, J.; Guo, X.; Wang, S.; Qu, B. Lead-free Double Perovskite Cs<sub>2</sub>AgIn<sub>0.9</sub>Bi<sub>0.1</sub>Cl<sub>6</sub> Quantum Dots for White Light-Emitting Diodes. *Adv. Sci.* **2022**, *9*, 2102895. [[CrossRef](#)]
189. Liu, Z.; Sun, Y.; Cai, T.; Yang, H.; Zhao, J.; Yin, T.; Hao, C.; Chen, M.; Shi, W.; Li, X.; et al. Two-Dimensional Cs<sub>2</sub>AgIn<sub>x</sub>Bi<sub>1-x</sub>Cl<sub>6</sub> Alloyed Double Perovskite Nanoplatelets for Solution-Processed Light-Emitting Diodes. *Adv. Mater.* **2023**, *35*, 2211235. [[CrossRef](#)]
190. Dohner, E.R.; Hoke, E.T.; Karunadasa, H.I. Self-Assembly of Broadband White-Light Emitters. *J. Am. Chem. Soc.* **2014**, *136*, 1718–1721. [[CrossRef](#)]
191. Dohner, E.R.; Jaffe, A.; Bradshaw, L.R.; Karunadasa, H.I. Intrinsic White-Light Emission from Layered Hybrid Perovskites. *J. Am. Chem. Soc.* **2014**, *136*, 13154–13157. [[CrossRef](#)] [[PubMed](#)]
192. Even, J.; Pedesseau, L.; Katan, C. Understanding Quantum Confinement of Charge Carriers in Layered 2D Hybrid Perovskites. *ChemPhysChem* **2014**, *15*, 3733–3741. [[CrossRef](#)] [[PubMed](#)]
193. Tyagi, P.; Arveson, S.M.; Tisdale, W.A. Colloidal Organohalide Perovskite Nanoplatelets Exhibiting Quantum Confinement. *J. Phys. Chem. Lett.* **2015**, *6*, 1911–1916. [[CrossRef](#)] [[PubMed](#)]
194. Jung, M.-C.; Raga, S.R.; Qi, Y. Properties and Solar Cell Applications of Pb-Free Perovskite Films Formed by Vapor Deposition. *RSC Adv.* **2016**, *6*, 2819–2825. [[CrossRef](#)]
195. Liao, Y.; Liu, H.; Zhou, W.; Yang, D.; Shang, Y.; Shi, Z.; Li, B.; Jiang, X.; Zhang, L.; Quan, L.N.; et al. Highly Oriented Low-Dimensional Tin Halide Perovskites with Enhanced Stability and Photovoltaic Performance. *J. Am. Chem. Soc.* **2017**, *139*, 6693–6699. [[CrossRef](#)] [[PubMed](#)]
196. Wang, S.; Li, X.; Wu, J.; Wen, W.; Qi, Y. Fabrication of Efficient Metal Halide Perovskite Solar Cells by Vacuum Thermal Evaporation: A Progress Review. *Curr. Opin. Electrochem.* **2018**, *11*, 130–140. [[CrossRef](#)]
197. Moghe, D.; Wang, L.; Traverse, C.J.; Redoute, A.; Sponseller, M.; Brown, P.R.; Bulović, V.; Lunt, R.R. All Vapor-Deposited Lead-Free Doped CsSnBr<sub>3</sub> Planar Solar Cells. *Nano Energy* **2016**, *28*, 469–474. [[CrossRef](#)]
198. Liu, M.; Johnston, M.B.; Snaith, H.J. Efficient Planar Heterojunction Perovskite Solar Cells by Vapour Deposition. *Nature* **2013**, *501*, 395–398. [[CrossRef](#)]
199. Yuan, F.; Xi, J.; Dong, H.; Xi, K.; Zhang, W.; Ran, C.; Jiao, B.; Hou, X.; Jen, A.K.Y.; Wu, Z. All-Inorganic Hetero-Structured Cesium Tin Halide Perovskite Light-Emitting Diodes with Current Density Over 900 A Cm<sup>-2</sup> and Its Amplified Spontaneous Emission Behaviors. *Phys. Status Solidi-Rapid Res. Lett.* **2018**, *12*, e2207454. [[CrossRef](#)]
200. Woo, J.Y.; Park, M.; Jeong, S.; Kim, Y.; Kim, B.; Lee, T.; Han, T. Advances in Solution-Processed OLEDs and Their Prospects for Use in Displays. *Adv. Mater.* **2023**. *early view*. [[CrossRef](#)]

**Disclaimer/Publisher's Note:** The statements, opinions and data contained in all publications are solely those of the individual author(s) and contributor(s) and not of MDPI and/or the editor(s). MDPI and/or the editor(s) disclaim responsibility for any injury to people or property resulting from any ideas, methods, instructions or products referred to in the content.